

2

AD-A263 073



ARMY RESEARCH LABORATORY



Navier-Stokes Simulation of Viscous, Separated, Supersonic Flow Over a Projectile Rotating Band

Bernard J. Guidos
James E. Danberg

ARL-TR-102

March 1993

DTIC
ELECTE
APR 21 1993
S B

APPROVED FOR PUBLIC RELEASE; DISTRIBUTION IS UNLIMITED.

93-08483



93 4 20 108

NOTICES

Destroy this report when it is no longer needed. DO NOT return it to the originator.

Additional copies of this report may be obtained from the National Technical Information Service, U.S. Department of Commerce, 5285 Port Royal Road, Springfield, VA 22161.

The findings of this report are not to be construed as an official Department of the Army position, unless so designated by other authorized documents.

The use of trade names or manufacturers' names in this report does not constitute indorsement of any commercial product.

REPORT DOCUMENTATION PAGE

Form Approved
OMB No 0704-0188

Public reporting burden for this collection of information is estimated to average 1 hour per response, including the time for reviewing instructions, searching existing data sources, gathering and maintaining the data needed, and completing and reviewing the collection of information. Send comments regarding this burden estimate or any other aspect of this collection of information, including suggestions for reducing this burden, to Washington Headquarters Services, Directorate for Information Operations and Reports, 1215 Jefferson Davis Highway, Suite 1204, Arlington, VA 22202-4302 and to the Office of Management and Budget, Paperwork Reduction Project (0704-0188), Washington, DC 20503.

1. AGENCY USE ONLY (Leave blank)		2. REPORT DATE March 1993	3. REPORT TYPE AND DATES COVERED Final, November 1989 - November 1991	
4. TITLE AND SUBTITLE NAVIER-STOKES SIMULATION OF VISCOUS, SEPARATED, SUPERSONIC FLOW OVER A PROJECTILE ROTATING BAND			5. FUNDING NUMBERS 1L162618AH80 62618A-00-001 AJ	
6. AUTHOR(S) BERNARD J. GUIDOS and JAMES E. DANBERG				
7. PERFORMING ORGANIZATION NAME(S) AND ADDRESS(ES) U.S. Army Research Laboratory ATTN: AMSRL-WT-PB Aberdeen Proving Ground, MD 21005-5066			8. PERFORMING ORGANIZATION REPORT NUMBER	
9. SPONSORING/MONITORING AGENCY NAME(S) AND ADDRESS(ES) US Army Research Laboratory ATTN: AMSRL-OP-CI-B (Tech Lib) Aberdeen Proving Ground, Maryland 21005-5066			10. SPONSORING/MONITORING AGENCY REPORT NUMBER ARL-TR-102	
11. SUPPLEMENTARY NOTES The report supersedes BRL-IMR-953, December 1990.				
12a. DISTRIBUTION/AVAILABILITY STATEMENT Approved for public release; distribution is unlimited.			12b. DISTRIBUTION CODE	
13. ABSTRACT (Maximum 200 words) A numerical simulation is made of the separated, turbulent flow over the rotating band of a projectile-like body at Mach numbers 2.5, 3.0, and 3.5. The simulation is made by solving the thin-layer, compressible, mass-averaged, Navier-Stokes equations using an implicit numerical procedure. Numerical solutions are generated on a body-conforming computational grid which is constructed by adapting the boundary conditions of a grid generation scheme which solves the two-dimensional Poisson equations. The computed surface pressure distributions are compared to existing supersonic wind tunnel measurements. An evaluation is made of the accuracy and suitability of the numerical approach, and recommendations are made for the direction of future investigation.				
14. SUBJECT TERMS Navier-Stokes Computations Fluid Dynamics Projectile Rotating Band			15. NUMBER OF PAGES 45	
			16. PRICE CODE	
17. SECURITY CLASSIFICATION OF REPORT UNCLASSIFIED	18. SECURITY CLASSIFICATION OF THIS PAGE UNCLASSIFIED	19. SECURITY CLASSIFICATION OF ABSTRACT UNCLASSIFIED	20. LIMITATION OF ABSTRACT UL	

INTENTIONALLY LEFT BLANK.

ACKNOWLEDGMENTS

The authors thank Dr. Walter B. Sturek and Dr. Jubaraj Sahu, both of the Army Research Laboratory, for reviewing this report. The authors also thank Dr. David Littlefield, formerly a post-doctorate at the Ballistic Research Laboratory, for providing an additional review of the manuscript.

Accession For	
BTIS GRA&I	<input checked="" type="checkbox"/>
DTIC TAB	<input type="checkbox"/>
Unannounced	<input type="checkbox"/>
Justification	
By _____	
Distribution/	
Availability Codes	
Dist	Avail and/or Special
A-1	

INTENTIONALLY LEFT BLANK.

TABLE OF CONTENTS

	<u>Page</u>
ACKNOWLEDGMENTS	iii
LIST OF FIGURES	vii
LIST OF TABLES	ix
1. INTRODUCTION	1
2. WIND-TUNNEL MEASUREMENTS	1
3. COMPUTATIONAL APPROACH	3
3.1 Parabolized Navier-Stokes (PNS)	3
3.2 Unsteady Navier-Stokes (UNS)	4
3.3 Flowfield Initialization for UNS	5
3.4 Other Numerical Aspects	6
4. COMPUTATIONAL GRIDS	6
5. RESULTS	9
5.1 Boundary Layer Displacement Thickness	9
5.2 Flow Structure	9
5.3 Surface Pressure Comparison	11
6. CONCLUSION	13
7. REFERENCES	35
APPENDIX: TABULATED SURFACE PRESSURE DATA	37
LIST OF SYMBOLS	41
DISTRIBUTION LIST	43

INTENTIONALLY LEFT BLANK.

LIST OF FIGURES

<u>Figure</u>		<u>Page</u>
1	Illustration of Wind-Tunnel Model and Rotating Band	15
2	Schlieren Photograph of Flow over Step-like Protuberance, $M=3.0$	16
3	UNS Computational Grid, $M=3.0$	17
4	UNS Computational Grid near Forward Face of Rotating Band, $M=3.0$	18
5	UNS Computational Grid near Rearward Face of Rotating Band, $M=3.0$	19
6	Computed Velocity Vectors near Forward Face, $M=3.0$	20
7	Computed Velocity Vectors near Rearward Face, $M=3.0$	21
8	Computed Mach Contours near Forward Face, $M=3.0$ (0.2 to 3.0 in increments of 0.1)	22
9	Computed Mach Contours near Rearward Face, $M=3.0$ (0.1 to 3.0 in incre- ments of 0.1)	23
10	Computed Mach Contours, $M=3.0$ (0.1 to 3.2 in increments of 0.1)	24
11	Computed Pressure Contours near Forward Face, $M=3.0$ (1.1 to 2.9 in incre- ments of 0.2)	25
12	Computed Pressure Contours near Rearward Face, $M=3.0$ (0.2 to 0.8 in incre- ments of 0.1)	26
13	Computed Pressure Contours, $M=3.0$ (0.1 to 3.0 in increments of 0.1)	27
14	Surface Pressure Comparison near Forward Face, $M=2.5$	28
15	Surface Pressure Comparison near Forward Face, $M=3.0$	29
16	Surface Pressure Comparison near Forward Face, $M=3.5$	30
17	Surface Pressure Comparison near Rearward Face, $M=2.5$	31
18	Surface Pressure Comparison near Rearward Face, $M=3.0$	32
19	Surface Pressure Comparison near Rearward Face, $M=3.5$	33

INTENTIONALLY LEFT BLANK.

LIST OF TABLES

<u>Table</u>		<u>Page</u>
1	Computed Boundary Layer Displacement Thicknesses at $x/d=4.35$	9
2	Computed Separation and Reattachment Distances (in Step Heights).	10

INTENTIONALLY LEFT BLANK.

1. INTRODUCTION

Spin is usually imparted to artillery shell during launch through the use of a rifled gun tube. Correspondingly, most shell configurations include a rotating band, which can be described as an axisymmetric step-like protuberance on the projectile which makes sliding contact with the rifling, transforming most of the resulting torque into a rolling motion of the shell. Such rolling motion is normally required to maintain stable atmospheric flight for projectiles which do not have lifting surfaces. One aerodynamic effect of the rotating band is an increase in the total drag of the shell, thought to be less than 5% (McCoy 1981).

A protuberance is defined here to be any physical irregularity of the projectile geometry (excluding the base) which has a noticeable influence on the flow. The projectile rotating band can be viewed as belonging to an extensive class of axisymmetric protuberances which are pertinent to many spinning and non-spinning projectile configurations. Other examples of axisymmetric protuberances include sabot grooves, buttress threads or grooves, and surface roughness in general.

The numerical prediction of the viscous flow over protuberances is an area of interest to the Army Research Laboratory (ARL). The simulation of the flow field through the application of *large-scale computational fluid dynamics (CFD)* techniques promises to be an accurate means for predicting the aerodynamic effects. The simulation of flow over a rotating band is made difficult by the presence of large flow gradients and separated flow regions.

In this study, simulation is made of the separated, turbulent flow over a step-like protuberance on a non-spinning body of revolution at Mach numbers 2.5, 3.0, and 3.5. A finite-difference numerical technique is used to solve the thin-layer, compressible, mass-averaged, Navier-Stokes equations. The numerical computation is performed on a non-orthogonal, metric-discontinuous, body-conforming grid. The computed surface pressure distributions are compared to existing supersonic wind-tunnel measurements at all three Mach numbers. Additional comparison is made with two previous computations of this case at Mach 3.0, and an evaluation is made of the accuracy and suitability of the CFD approach.

2. WIND-TUNNEL MEASUREMENTS

Experimental measurements have been made of the surface pressure near a step-like protuberance on a non-spinning axisymmetric body in a supersonic blow-down tunnel located at the U.S. Army Edgewood Research Development and Engineering Center, Edgewood,

Maryland (Danberg and Palko 1986). The wind-tunnel model, Figure 1, is a cone-cylinder configuration. The diameter of the cylinder, d , which is taken as the reference length, is 2.54 cm. The length of the model is approximately 6.8 calibers (1 cal = 1 reference length). The half-angle of the cone is 13.1°. Five pressure taps were installed in a row along a constant circumferential location on the the cylinder.

The step-like protuberance, also in Figure 1, is a ring of inner diameter 1.0 cal, outer diameter 1.04 cal, and width 0.505 cal. The ring was designed with a set screw in order to fasten it to a keyway inscribed along the cylinder. The ring, positioned approximately 5 cal from the nosetip, could be moved relative to the pressure taps so that measurements could be made at a large number of locations near the band. The pressure taps were located on the opposite side of the cylinder from the keyway. Measurements were made both with and without the protuberance.

The wind-tunnel model was supported at the base by an axial support and held fixed relative to the free stream. All measurements were made with the model positioned at 0° incidence. The stagnation temperature was 260 K. The average Reynolds number based on model diameter was 1.23, 1.33, and 1.42 million at Mach 2.5, 3.0, and 3.5, respectively. Data were taken only after the initial transient had decayed, implying that, since the model was thin-walled, the wall temperature was nearly adiabatic. Boundary layer transition was initiated through the use of a trip ring installed 1 cal from the nosetip, although the entire flow field was assumed to be fully turbulent in the computational simulations. A complete tabulation of the experimental data is given in the Appendix.

Figure 2 is a reproduction of a Schlieren photograph of the cylinder portion of the wind-tunnel model, including the protuberance, at Mach 3. The density gradients are exposed as contrasting shades of light. The compression waves coalesce into weak shock waves which emanate from the forward and rearward faces of the protuberance. An additional series of compression waves upstream of the protuberance emanate from the keyway which secures the ring to the cylinder, contaminating a portion of the flow. The pressure taps are located on the opposite side of the cylinder, though, and should not be affected.

3. COMPUTATIONAL APPROACH

An unsteady Navier-Stokes (UNS) technique is used to compute the flow in the vicinity of the rotating band. The UNS technique solves the governing equations by integrating through time toward a steady-state solution. Inflow conditions upstream of the rotating band are provided by a separate computation which utilizes a parabolized Navier-Stokes (PNS) technique. The PNS technique computes the flow by integrating (marching) in the streamwise direction. A brief description of both is included here, and the references may be consulted for additional details.

The use of the PNS and UNS techniques in conjunction is an efficient way to model the flow. The PNS technique, which processes only two physical planes of data simultaneously, is applied over the cone and cylinder upstream of the rotating band, where the flow is attached. The UNS technique, which is more computationally intensive, is applied over the rotating band, where separated flow regions exist.

3.1 Parabolized Navier-Stokes (PNS). Computational modeling of the flow over the cone-cylinder is accomplished using the PNS technique first reported by Schiff and Steger (1979). This technique spatially integrates the dimensionless, transformed, steady, thin-layer, mass-averaged Navier-Stokes equations in strong conservation law form, given as:

$$\hat{E}_{\xi} + \hat{F}_{\eta} + \hat{G}_{\zeta} = \hat{R}e^{-1} \hat{S}_{\zeta} \quad (1)$$

Equation (1) represents steady-state conservation of mass, momentum, and energy in transformed coordinates for large Reynolds number flows. \hat{E}_{ξ} , \hat{F}_{η} , and \hat{G}_{ζ} are the transformed inviscid flux vectors. \hat{E}_{ξ} is a modified flux vector resulting from the subsonic sublayer approximation. The vector \hat{S}_{ζ} is the transformed vector of viscous terms that results from the thin-layer approximation. Perfect gas behavior is assumed. The transformed coordinates are: $\xi = \xi(x)$, the axial (marching) coordinate; $\eta = \eta(x, y, z)$, the circumferential coordinate; and $\zeta = \zeta(x, y, z)$, the radial coordinate.

The vector of dependent variables is defined as

$$\bar{Q} = [\rho, \rho u, \rho v, \rho w, \varepsilon]^T \quad (2)$$

where the density is ρ ; the velocity components in the x , y , and z directions are u , v , and w , respectively; and the total energy per unit volume is ε . The solution is obtained at each grid point using the approximately factored, implicit, delta-form, finite-difference

algorithm of Beam and Warming (1978). Second-order central-differencing is used in the circumferential and radial directions, and first-order one-sided differencing is used in the marching direction. Fourth-order explicit smoothing is added to suppress high frequency oscillations in the solution. The solution is advanced downstream by numerically integrating in the direction parallel to the projectile axis. Each marching step requires a series of block tridiagonal matrix inversions (sweeps) in the circumferential and radial directions.

At the body surface, the no-slip condition is enforced and the pressure is obtained from the subsonic sublayer approximation (i.e., the pressure across the subsonic portion of the viscous layer is held constant). The outer boundary, which consists of the bow shock, is shock fitted using an implicit procedure (Rai and Chaussee 1983). Initial conditions for marching are generated using the PNS method in step-back mode (Rai and Chaussee 1983; Schiff and Sturek 1981; Weinacht et al. 1985), which assumes conical flow conditions near the nosetip and iteratively refines the solution to satisfy this assumption.

The PNS computations provide inflow conditions for the ensuing UNS computations. The dependent flow variables are linearly interpolated onto the UNS computational grid 15 step heights upstream of the protuberance. Additionally, the PNS method was used in earlier portions of this study to verify the integrity of the measured pressures without a protuberance (Danberg and Palko 1986), and to attempt a simplified ramp model to approximate the rotating band flowfield (Danberg 1983).

Turbulence is accounted for in both the PNS and UNS computations using the two-layer, algebraic eddy viscosity model of Baldwin and Lomax (1978). The inner wall-layer eddy viscosity is computed using a conventional Prandtl mixing length and Van Driest damping. The outer or wake layer viscosity is based on evaluating the maximum in the moment of vorticity and its normal distance from the wall. The calculation of the eddy viscosity is lagged by one time step in the UNS code and by one marching step in the PNS code.

3.2 Unsteady Navier-Stokes (UNS). Computational modeling of the flow over the rotating band is accomplished using the UNS approach first reported by Pulliam and Steger (1978). This technique temporally integrates the dimensionless, transformed, time-dependent, thin-layer, mass-averaged, Navier-Stokes equations in strong conservation law form, given as:

$$\hat{Q}_\tau + \hat{E}_\xi + \hat{F}_\eta + \hat{G}_\zeta = \hat{R}e^{-1} \hat{S}_\zeta \quad (3)$$

Equation (3) represents conservation of mass, momentum, and energy in transformed

coordinates for large Reynolds number flow. The vector \hat{Q} is the transformed vector of dependent variables. The vectors \hat{E} , \hat{F} , and \hat{G} are the transformed inviscid flux vectors. The vector \hat{S} is the transformed vector of viscous terms that result from the thin-layer approximation for large Reynolds number flows. Ideal gas behavior is assumed. The transformed coordinates are : $\tau = t$, time; $\xi = \xi(t, x, y, z)$, the longitudinal (streamwise) coordinate; $\eta = \eta(t, x, y, z)$, the circumferential coordinate; and $\zeta = \zeta(t, x, y, z)$, the near-normal coordinate.

The vector of dependent variables, given in Eq. (2), is obtained at each grid point using the approximately factored, implicit, delta-form, finite-difference algorithm of Beam and Warming (1978). Second-order central-differencing is used in the three coordinate directions. and first-order, one-sided time differencing is used. The solution at each time step requires a series of block-tridiagonal matrix inversions (sweeps) in each of the transformed coordinate directions. Fourth-order explicit and second-order implicit smoothing terms are added to suppress high frequency oscillations in the solution.

On the body surface, the no-slip boundary condition is enforced. The surface pressure is found by assuming a zero normal gradient at the wall. The density and energy are found by assuming adiabatic wall conditions. For a constant coefficient of thermal conductivity, this condition translates into a zero density gradient in the normal direction, and was applied as a first-order approximation in the ζ direction. On the outer boundary, the dependent flow variables are assumed free stream. On the outflow boundary, the dependent flow variables are determined using linear extrapolation along constant η and ζ grid lines, which corresponds to a constant outflow gradient boundary condition. Axisymmetry is invoked applying the procedure reported by Rizk, Chaussee, and McRae (1982), which employs three circumferential grid planes. Turbulence is accounted for using the algebraic eddy viscosity model of Baldwin and Lomax (1978).

3.3 Flowfield Initialization for UNS. Flowfield initialization proved to be an important consideration for ensuring numerical stability in the early stages of the time-dependent computations. It is well-known that the best initial flow field is one which somewhat resembles the final, converged solution. The first initialization scheme attempted here (beyond a simple free-stream initialization, which was inadequate) was of the form

$$\bar{Q}_{i,j,k} = \bar{Q}_{1,j,k} \quad (4)$$

where the indices i, j , and k represent grid nodes in the ξ, η , and ζ directions, respectively. That is, the flow variables at each k (outward) index were assigned values from the corresponding k index at the inflow boundary. This initialization was found to be inadequate because the computed solution quickly formed a large flow discontinuity along the forward

face of the protuberance, resulting in numerical instability.

To overcome this problem, the initial u velocity components of the the first flowfield initialization were made more incipient, or ready to separate, by multiplying u at each grid point downstream of the inflow boundary by a factor f_k , i.e.,

$$(u_{i,j,k})_{new} = (u_{i,j,k})_{old} f_k \quad (5)$$

where

$$f_k = \begin{cases} \frac{k-1}{k_{mid}-1} & \text{for } k \leq k_{mid} \\ 1.0 & \text{for } k > k_{mid} \end{cases} \quad (6)$$

The index k_{mid} was set equal to approximately half of k_{max} . This re-initialization procedure was sufficient to allow the solution to remain numerically stable.

3.4 Other Numerical Aspects. The numerical computations were performed on a Cray X-MP/48 computer located at the Ballistic Research Laboratory. Each computation required 322 thousand words, or 2.576 million bytes, of computer memory. The computer speed was approximately 3 seconds per integration step using a 140 x 65 computational grid. Approximately 3 hours of computer time were used to advance each numerical solution through 3500 integration steps. Additional integration steps were made but did not change the solutions appreciably.

The time increment, Δt , was determined by specifying a maximum allowable Courant number, C_t , in the computational domain (Kutler, Chaussee, and Lombard 1978). The initial value of C_t was set at 5.0 initially, and slowly raised to a value of 20.0 by 3500 time steps. The values of the smoothing parameters ϵ_i and ϵ_e (implicit and explicit, respectively) were set at 0.1 and 0.05 initially, and lowered to 0.06 and 0.03 after 3500 time steps. No attempt was made to examine the effect of various combinations of time step and smoothing parameters.

4. COMPUTATIONAL GRIDS

A major point of interest is the applicability of a grid that "wraps around" the step-like protuberance. For this problem, such an approach requires the construction of a highly skewed grid in regions of sharp surface discontinuities.

The grid is generated using a technique based on the well-known work of Thompson, Thames, and Mastin (1974). The governing equations are the Poisson equations in two

dimensions:

$$\begin{aligned}\xi_{xx} + \xi_{yy} &= P(\xi, \zeta) \\ \zeta_{xx} + \zeta_{yy} &= Q(\xi, \zeta)\end{aligned}\tag{7}$$

In this set of elliptic equations, $\xi = \xi(x, y)$ and $\zeta = \zeta(x, y)$ are the transformed coordinates. The inhomogeneous terms P and Q are forcing functions which control the point spacing throughout the interior of the domain.

Steger and Sorenson (1979) implemented new boundary conditions to the governing equations to achieve two effects: (1) to cluster points at a specified distance from a boundary, and (2) to force grid lines to intersect the boundary at a specified angle. Their approach restricts the application of the forcing terms P and Q to the wall boundary ($\zeta = \zeta_1$), which somewhat simplifies the equations and adds additional control to the grid at the wall boundary. Their condition that grid lines intersect the inner boundary in a specified fashion is obtained using the relation

$$\nabla \xi \cdot \nabla \zeta = |\nabla \xi| |\nabla \zeta| \cos \theta\tag{8}$$

where ∇ is the gradient and θ is the orthogonality angle, defined here as the angle between a constant ζ line and a constant ξ line. Using the transform relations ($\xi_x = y_c/J$, etc., where J is the Jacobian of the transformation), this condition becomes

$$x_\xi x_\zeta + y_\xi y_\zeta = - \left[(x_\zeta^2 + y_\zeta^2)(x_\xi^2 + y_\xi^2) \right]^{1/2} \cos \theta\tag{9}$$

where θ is specified along the wall boundary.

The grid generation scheme was modified here to control θ along the wall by defining it as a function of x/d . To allow such a function to exist along the vertical faces of the rotating band, the bottom corner of the forward face of the protuberance was shifted upstream by 0.001 cal, from $x/d=4.95$ to $x/d=4.949$. The change in vertical orientation of the forward face due to this shift is approximately 1.43° , and is not expected to change the flow field from that of a vertical face (Young and Paterson 1981). The orthogonality angle along the wall was prescribed upstream of the midpoint of the band; downstream of the midpoint, the

grid was constructed using reflection principles. The orthogonality angle was prescribed as:

$$\theta = \begin{cases} \frac{\pi}{2} - \frac{\pi (x/d - 4.35)}{4 (4.494 - 4.35)} & \text{for } 4.35 \leq x/d < 4.949 \text{ (upstream of band)} \\ \frac{\pi}{2} & \text{for } x/d = 4.949 \text{ (bottom front corner grid point)} \\ \frac{3\pi}{4} & \text{for } 4.949 < x/d < 4.95 \text{ (front face of band)} \\ \frac{\pi}{2} & \text{for } x/d = 4.95 \text{ (top front corner grid point)} \\ \frac{\pi}{2} + \frac{\pi (5.20 - x/d)}{4 (5.20 - 4.95)} & \text{for } 4.95 < x/d < 5.20 \text{ (top front half of band)} \end{cases} \quad (10)$$

The computational grid used for the Mach 3.0 case is shown in Figure 3. In the longitudinal direction, 140 grid points were used. In the outward direction, 65 grid points were used. The grid does not change with time. The inflow boundary is located at $x/d=4.35$, or 15 step heights upstream of the forward face of the protuberance. The outflow boundary is located at $x/d=6.05$, or 15 step heights downstream of the rearward face of the protuberance.

Figures 4 and 5 show closeup views of the computational grid at the forward and rearward faces of the protuberance. As usual for viscous computations, the grid is clustered near the wall. The distance between the wall and the first outward grid point is held constant for each case. The values were obtained from the corresponding PNS solution at the inflow plane, which, through an adaptive grid technique (Sturek and Schiff 1981), maintained the outward spacing at the wall such that the first grid point from the wall satisfied the condition $3 \leq y^+ \leq 5$. The longitudinal point distribution is prescribed such that grid points were slightly clustered along the forward and rearward faces. Each face contains 9 grid points, including the top and bottom corners.

Appreciable discontinuities in the grid metrics extend outward from the top and bottom corners of each face. The grid is highly skewed in these regions, at about 45° . Grid non-orthogonality at the wall is an issue of interest since the wall boundary conditions are implemented with the assumption that the grid is orthogonal to the wall. The effective error is expected to be small due to small grid spacing in the outward direction as well as the small longitudinal gradients (compared to the outward gradients) which occur at the wall.

5. RESULTS

5.1 Boundary Layer Displacement Thickness. The relative sizes of the incoming boundary layers with respect to the rotating band thickness give an indication of the scale of the problem (Sedney 1973). The boundary layer displacement thickness, δ^* , was determined from the converged numerical solutions 15 step-heights upstream of the rotating band. A compressible, axisymmetric boundary layer was assumed; the displacement thickness was calculated using

$$\delta^* = \sqrt{2 \int_{r_w}^{r_e} \left(1 - \frac{\rho u}{\rho_e u_e}\right) r dr} + r_w^2 - r_w \quad (11)$$

where the subscripts w and e represent wall and edge conditions, respectively. At each Mach number, a variation of δ^* was generated as a function of assumed edge location. The u_e profiles were inspected and found to be well-behaved. The displacement thickness was maximum near the apparent boundary layer edge and the edge location was assumed to occur at this maximum. The accuracy of the predicted δ^* is within 1%; the determined values are shown in Table 1. The table shows that, in each case, the computed displacement thickness is about half of the rotating band thickness.

Table 1. Computed Boundary Layer Displacement Thicknesses at $x/d=4.35$.

M	δ^* (cal)
2.5	$0.0159 \pm 1\%$
3.0	$0.0186 \pm 1\%$
3.5	$0.0226 \pm 1\%$

5.2 Flow Structure. Figures 6 and 7 show computed velocity vectors for the Mach 3 case near the forward and rearward faces of the rotating band, respectively. Longitudinally-separated flow regions are captured in the numerical solution both upstream and downstream of the band. The computed separation and reattachment points were more precisely determined at each Mach number by examining the computed skin friction coefficient. The velocity derivative used to compute the skin friction was approximated using a one-sided, first-order difference. The skin friction was assumed to vary linearly between adjacent grid points; separation or reattachment was assumed to occur where the skin friction was zero. Table 2 shows the computed separation and reattachment distances for each of the three different Mach numbers. The separation distance is computed to vary by less than 1% between the three Mach numbers. The non-monotonic variation of separation distance with respect

to Mach number is likely within the accuracy of the computation, given the current longitudinal grid resolution and the assumptions used to compute skin friction and separation location.

Table 2. Computed Separation and Reattachment Distances (in Step Heights).

M	$(s_a - s_{sep})/h$	$(s_{reat} - s_b)/h$
2.5	5.05	3.99
3.0	5.03	3.59
3.5	5.09	3.37

Figures 8 and 9 show the computed Mach contours in the forward and backward step regions for the Mach 3.0 case. The sonic line is emphasized. Only slight jaggedness in the Mach contours are discernible along the constant ξ grid lines which emanate from the top and bottom corners of the faces, where large metric discontinuities exist. Figure 10 shows computed Mach contours for the entire computational domain. The crispness of the weak shocks in the far field is definitely limited by the poor grid resolution there. The compression which emanates from the front face is consistently captured between three adjacent grid points, but far from the body such capturing still gives a largely smeared structure. The recompression just downstream of the rearward face appears to be captured slightly better, possibly because of better grid resolution there. The computed bow shock is also smeared downstream from the inflow boundary, and the disturbances propagate toward the body and interact with the waves which emanate from the rotating band. The influence of these outer disturbances on the computed flow field near the rotating band is thought to be negligible: first, the characteristic lines are not of sufficient slope to intersect the body close to the band, and second, the flow is nearly uniform in the outer region.

Figures 11 and 12 show the computed pressure contours in the forward and backward step regions for the Mach 3.0 case. The contours are plotted as p/p_∞ . The highest surface pressure on the front face, occurring near the top of the band, is computed to be 2.91. The stagnation region appears to be spread over several grid points, rather than being concentrated at a particular point. Some jaggedness is present in the contours near the top corner of the forward face. The lowest surface pressure on the rearward face, occurring near the top of the band, is computed to be 0.104. The computed expansion begins at about two grid points upstream of the corner of the rearward face ($x/d \approx 5.435$), indicating that flow disturbances are being propagated upstream through the subsonic portion of the boundary layer. Jaggedness in the contours near the top corner of the rearward face is not nearly as apparent as that near the forward face, possibly because the gradients are not as

large. Figure 13 shows computed pressure contours for the entire computational domain. The contour which runs nearly parallel and next to the outer boundary is the level 1.1, and represents the captured outer bow shock.

5.3 Surface Pressure Comparison. The pressure is compared in the form ΔC_p , which is the difference in surface pressure coefficient with and without the rotating band, i.e.,

$$\Delta C_p = C_{p_1} - C_{p_0} = \frac{p_1/p_\infty - p_0/p_\infty}{\frac{1}{2}\gamma M^2} \quad (12)$$

where p_1 and p_0 are the surface pressures with and without the band, respectively. The formal accuracy of the pressure measurements is discussed in detail in the experiment documentation (Danberg and Palko 1986). The repeatability of the measured ΔC_p appears to be approximately 0.01 .

The surface pressure distributions are plotted as functions of distance along the surface coordinate, s (which is coincident with ξ), scaled by the band height, h . The origin of s for comparisons upstream of the band is s_a , located at the bottom corner of the forward face. The origin of s for comparisons downstream of the band is s_b , located at the bottom corner of the rearward face. The final, tabulated data is listed in the Appendix.

Upstream of the rotating band, Figures 14-16, the computed and measured pressures compare to within about 0.01 in the attached flow region at all three Mach numbers. In all three cases, the location of initial pressure rise associated with the onset of flow separation is predicted to occur further upstream than the measurements show. Near this location, the computed ΔC_p is as much as 0.03 greater than the measured value. At about 2 to 4 step heights upstream of the band, the difference in the computed and measured ΔC_p is within 0.01. At less than 2 step heights upstream of the band, the computation overpredicts ΔC_p to a maximum of about 0.04 at Mach 2.5 and 3.0. At Mach 3.5, the computation overpredicts ΔC_p to a maximum of about 0.02.

Downstream of the rotating band, Figures 17-19, the computed and measured pressures compare quite differently than upstream of the band. Within 1 step height downstream of the band, the computed and measured pressures agree within about 0.015. However, the experiment shows a rapid pressure recovery 2 to 4 step heights downstream of the face, whereas the computation shows a slow pressure recovery extending beyond 8 step heights downstream. This trend is repeated at all three Mach numbers.

Figures 15 and 18 include the results of a previous computation of the Mach 3.0 case (Sahu 1986). Those results were generated using the same numerical scheme as in this study, but

with some important differences in the approach. The first difference is that the computation was carried out on an orthogonal grid, as opposed to the highly skewed grid of this study. Second, the no-slip boundary condition was applied along the forward and rearward step faces by using a flowfield blanking procedure. Third, the Baldwin-Lomax turbulence model was only applied along grid lines which emanated from the cylinder surface, meaning that the effective turbulence was not adequately specified along the forward and rearward step faces. Fourth, the longitudinal grid resolution in the separated flow regions was not as good as in this study. In Figures 15 and 18, the two computational results are similar in that they agree with some, but not all, of the measured pressures upstream of the band. Close to the forward face, the prediction of the present study appears to agree with the measured pressure slightly better than that of Sahu. Atop of the band, the computations disagree with each other, but the prediction of the present study appears to agree better with the single available data point. Downstream of the band, both computations fail to predict the rapid pressure recovery that occurs from 1 to 3 step-heights downstream. Sahu's computation shows a faster pressure recovery than the present computation, but this is likely due to its higher pressure atop of the band itself. No comparison can be made on the vertical faces of the band, since Sahu's values are no longer available and were never published.

Still another computation of the Mach 3.0 case has been reported (Danberg and Patel 1989). Those results were generated by solving the full, mass-averaged Navier-Stokes equations using a zonal, explicit numerical approach on an orthogonal grid. The Baldwin-Lomax turbulence model was used in a modified form. Through an examination of the reported pressure distribution, it is easily determined that agreement with the measured surface pressure was quite similar to the present computation and to that of Sahu. Upstream of the band, the pressure near the forward face is overpredicted. Downstream of the band, the rapid pressure recovery is not predicted.

The three independent computational results suggest that the thin-layer model and the highly skewed grid are not major sources of error in the present study. The experimental measurements are assumed to be accurate. It is concluded the turbulence model is the most likely contributor to inaccuracies in the computed pressure field in this study, as well as in the other two studies.

The inaccuracy of the computed recovering pressure field downstream of the band raises some concern for the applicability of the CFD approach. The current CFD capability may have value for predicting the drag due to the presence of the rotating band, although confirmation of this has not yet been made. Experimental drag data with and without a rotating band would be valuable. The computed recovering boundary layer is probably no more accurate than the computed recovering pressure field. Computations of, for instance, Mag-

nus effects (which are critically dependent on the boundary layer profile) would need to be validated. The velocity data which has been published by Gorney, Yanta, and Ausherman (1982) may be valuable for validating the accuracy of the computed attached, recovering boundary layer downstream of the band.

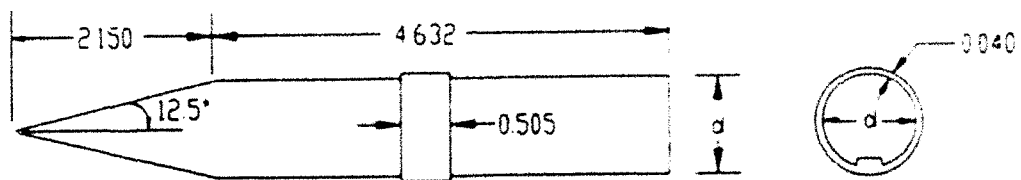
6. CONCLUSION

The numerical solution showed the displacement thickness of the oncoming boundary layer to be the same order of magnitude as the step height. Regions of flow separation were captured in the numerical solutions. In the recirculation region upstream of the protuberance, agreement in computed and measured pressures was within the measurement accuracy at most tap locations. Near the predicted separation point and within 2 step heights of the forward face, agreement was not within the measurement accuracy. In the interaction region downstream of the protuberance, agreement was within the measurement accuracy only within 1 step height from the rearward face, and the rate of pressure recovery was underpredicted in the numerical solutions. The pressure comparison upstream of the protuberance was significantly better than the comparison downstream of the protuberance.

A highly skewed, metric-discontinuous, wrap-around grid was used to perform the computations. Except for some minor jaggedness in the pressure contours, no major discontinuities can be discerned in the numerical solution where the grid metrics change rapidly. Two other CFD studies which did not use highly skewed grids were found to have similar disagreement in surface pressure as this study. Under these considerations, the non-orthogonal, metric-discontinuous grid does not appear to be an obvious cause of solution inaccuracies. A more likely contributor to inaccuracies in the computed solutions of all three studies is the Baldwin-Lomax algebraic turbulence model, which has been employed here without modification.

Further study in the modeling of separated flow over protuberances will need to address the issue of turbulence modeling in detail. Higher order models may be needed to improve the accuracy of the numerical prediction. Attention should be given to the accuracy of the reattached, recovering boundary layer downstream of the rotating band. An experimental consideration of the drag increase due to the rotating band would be of tremendous value to evaluate CFD models. An extension of the present work could include a substantial increase in grid resolution; the present grid resolution was chosen to roughly match that of the two previous computational studies which were cited.

INTENTIONALLY LEFT BLANK.



All Dimensions in Calibers
 Diameter, $d=2.54\text{cm}$

Figure 1. Illustration of Wind Tunnel Model and Rotating Band

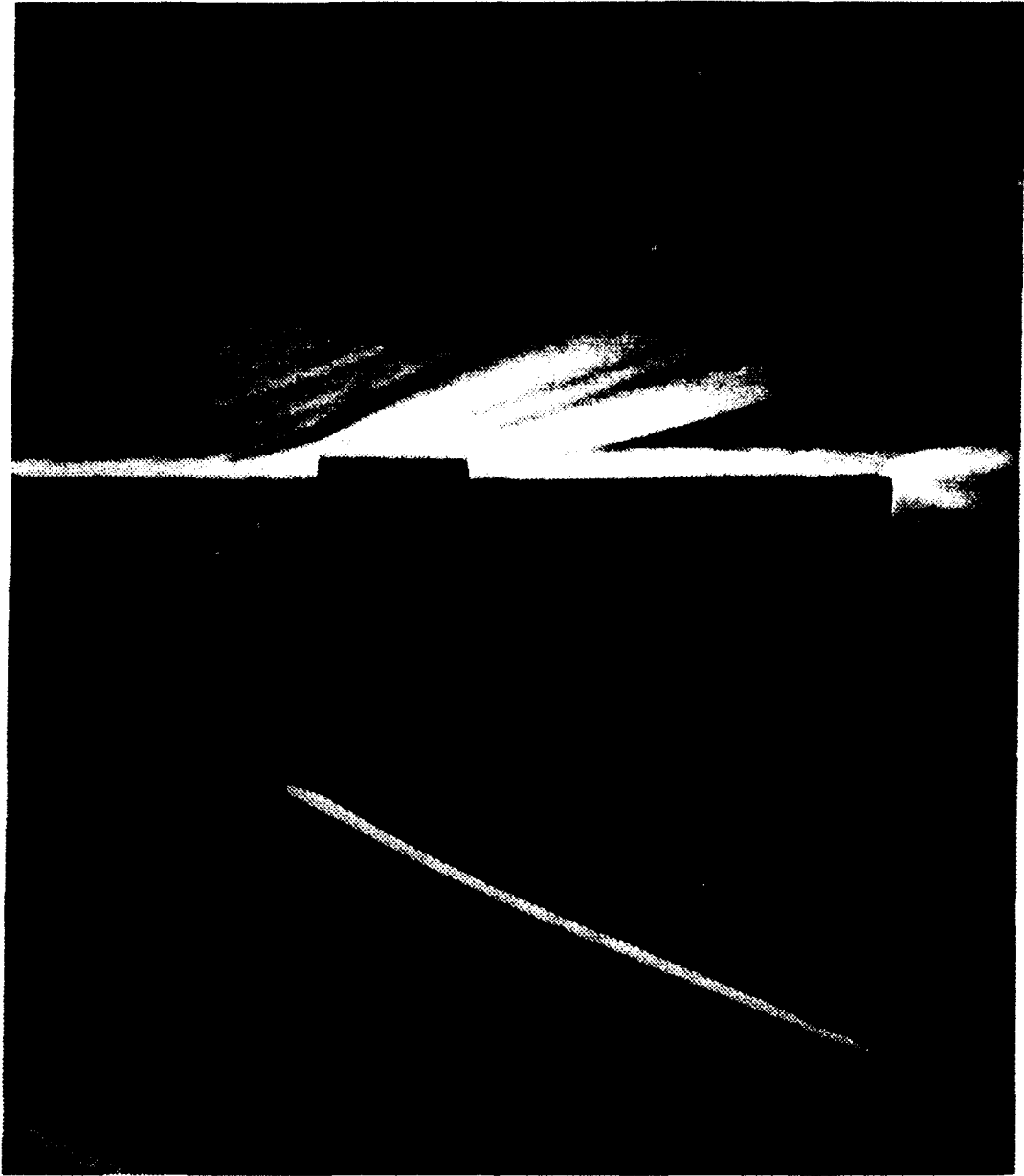


Figure 2. Schlieren Photograph of Flow over Step-like Protuberance at Mach 3

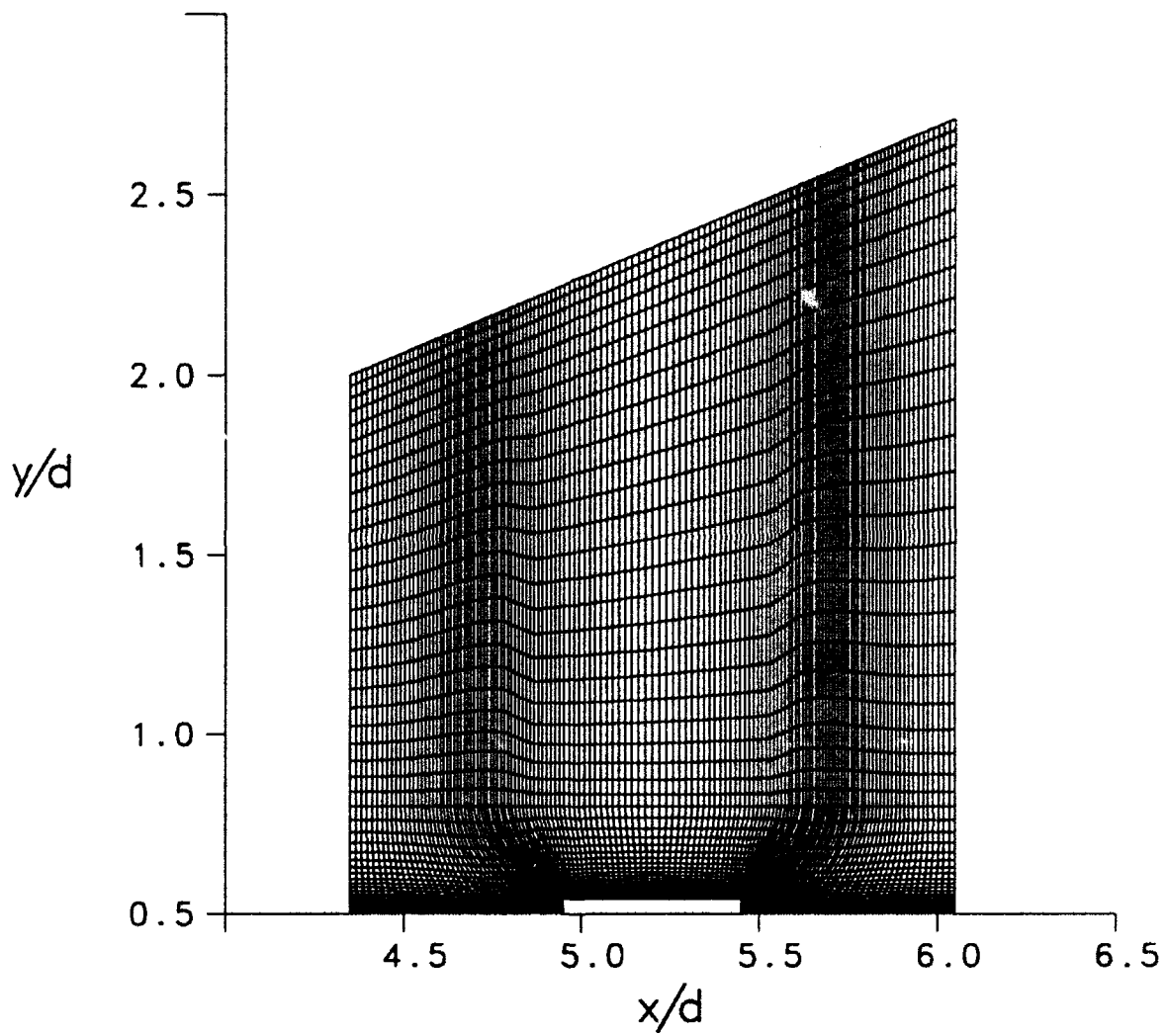


Figure 3. UNS Computational Grid, $M=3.0$

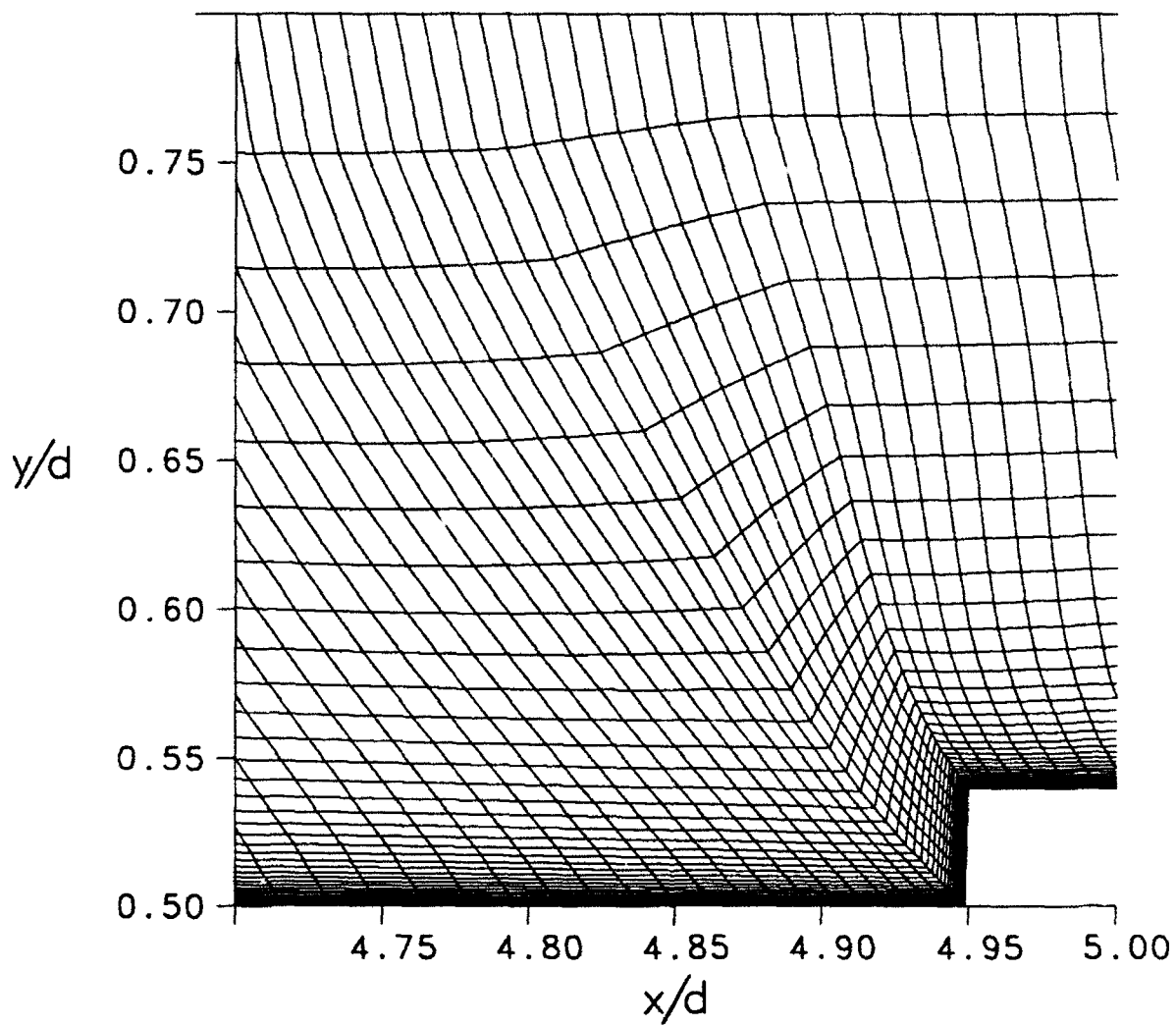


Figure 4. UNS Computational Grid near Forward Face of Rotating Band, $M=3.0$

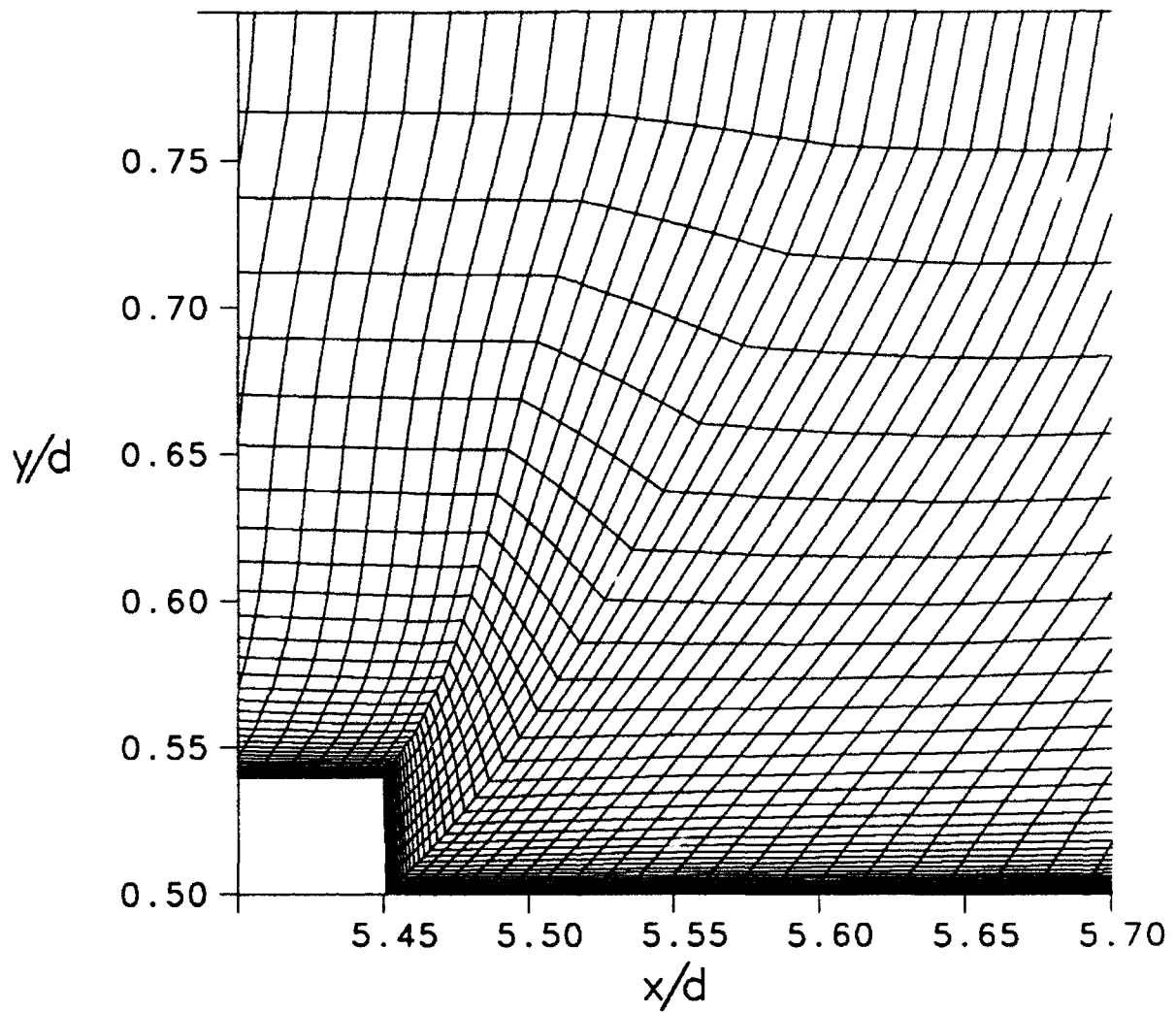


Figure 5. UNS Computational Grid near Rearward Face of Rotating Band, $M=3.0$

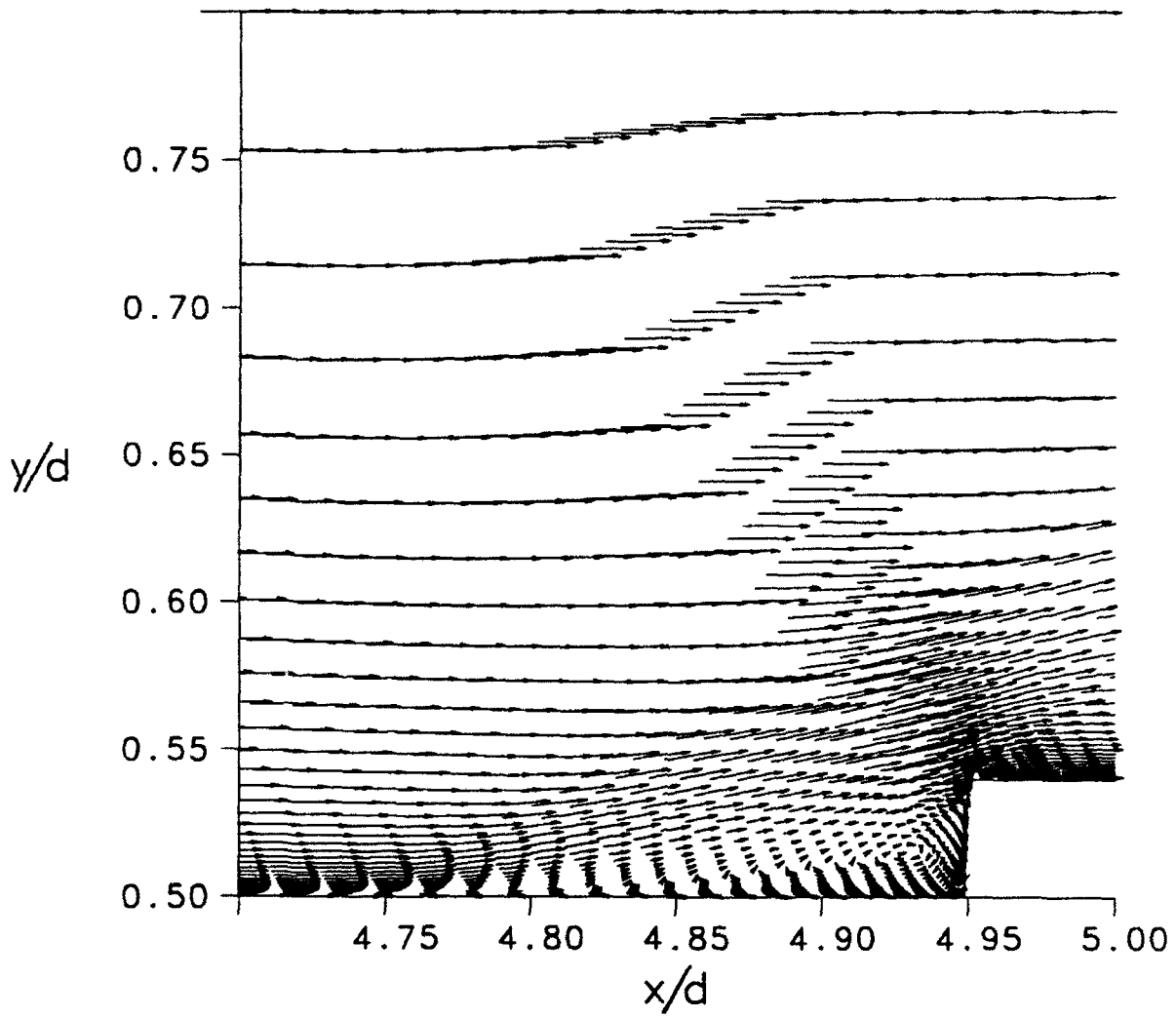


Figure 6. Computed Velocity Vectors near Forward Face, $M=3.0$

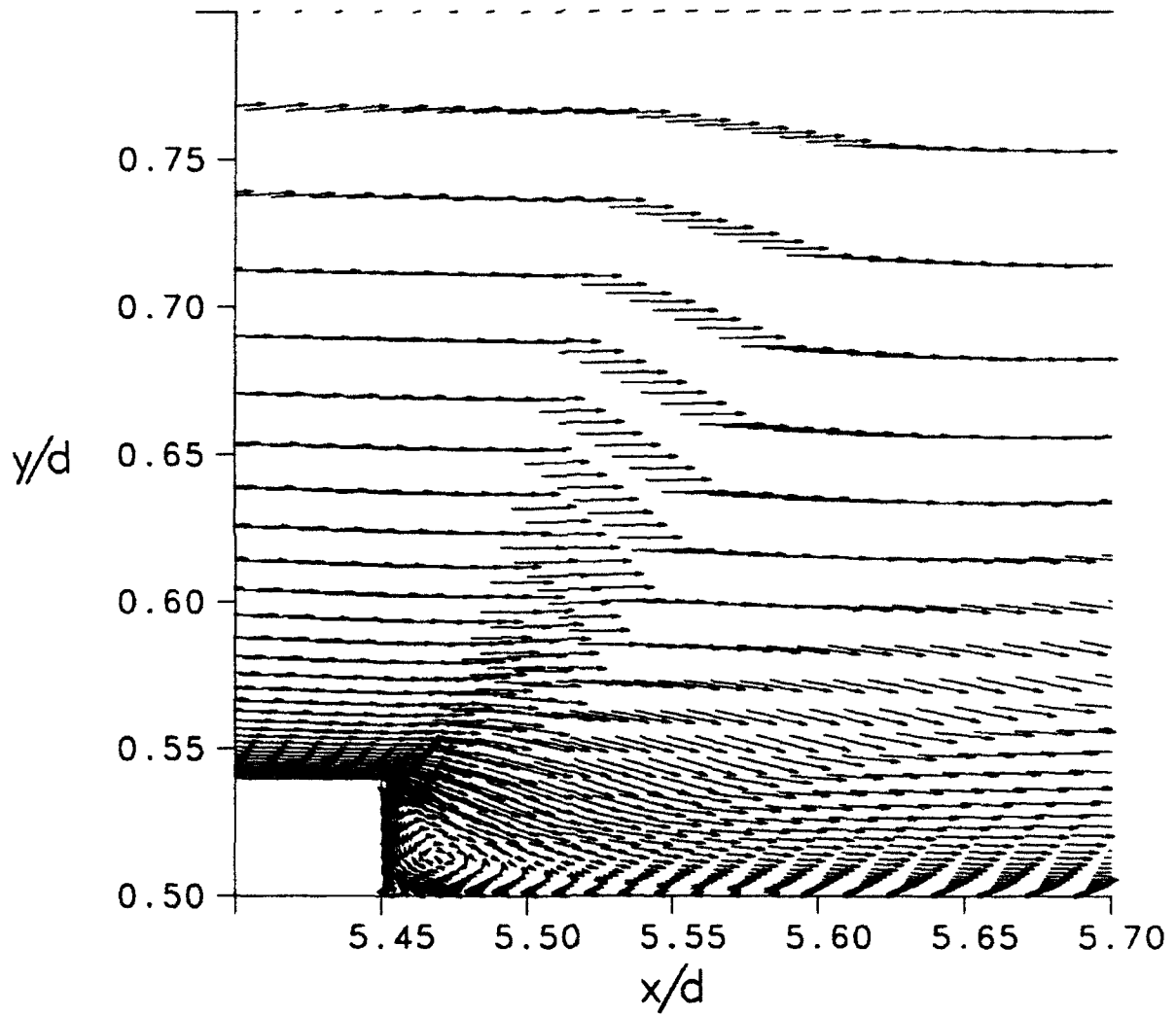


Figure 7. Computed Velocity Vectors near Rearward Face, $M=3.0$

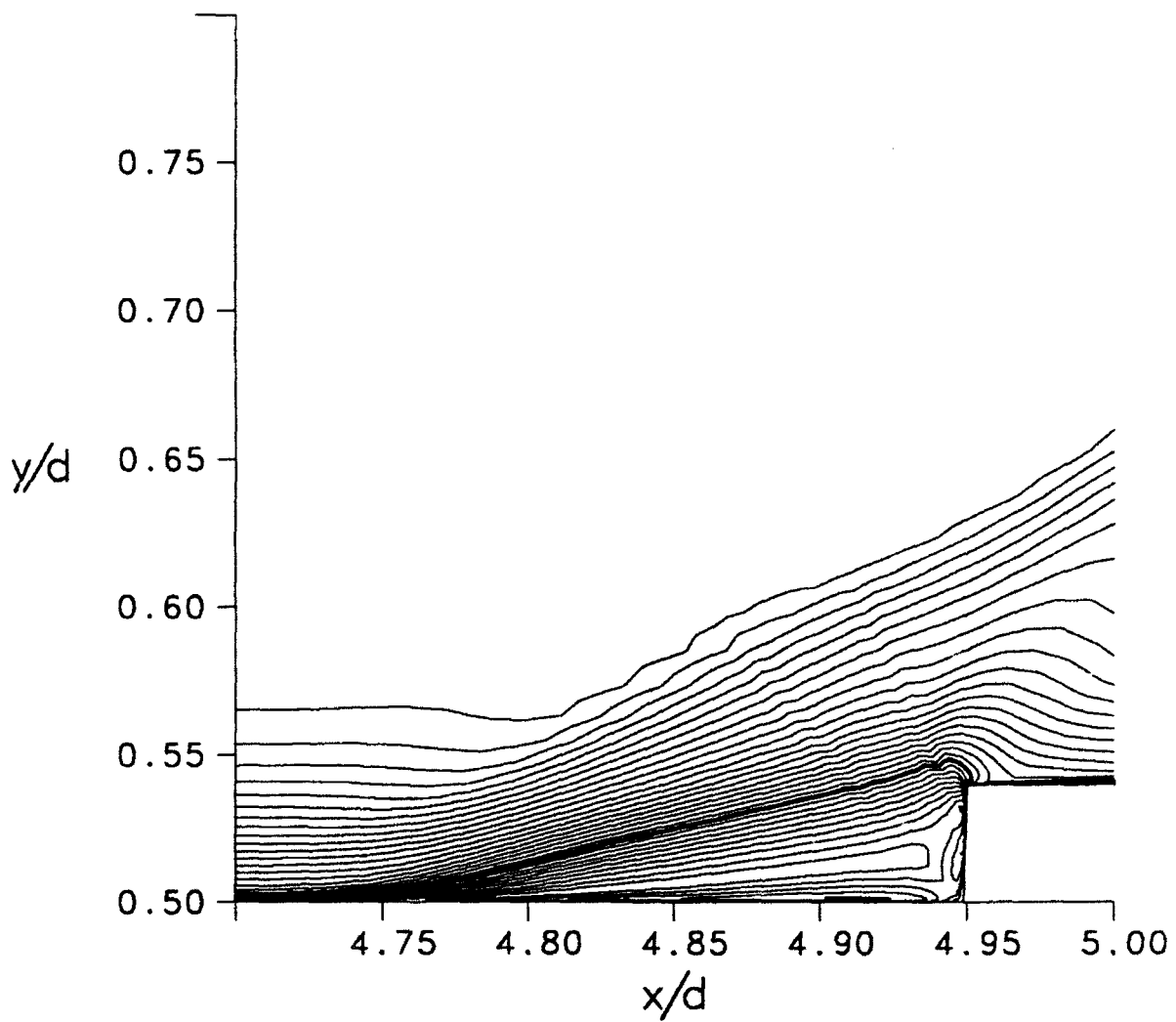


Figure 8. Computed Mach Contours near Forward Face, $M=3.0$ (0.2 to 3.0 in increments of 0.1)

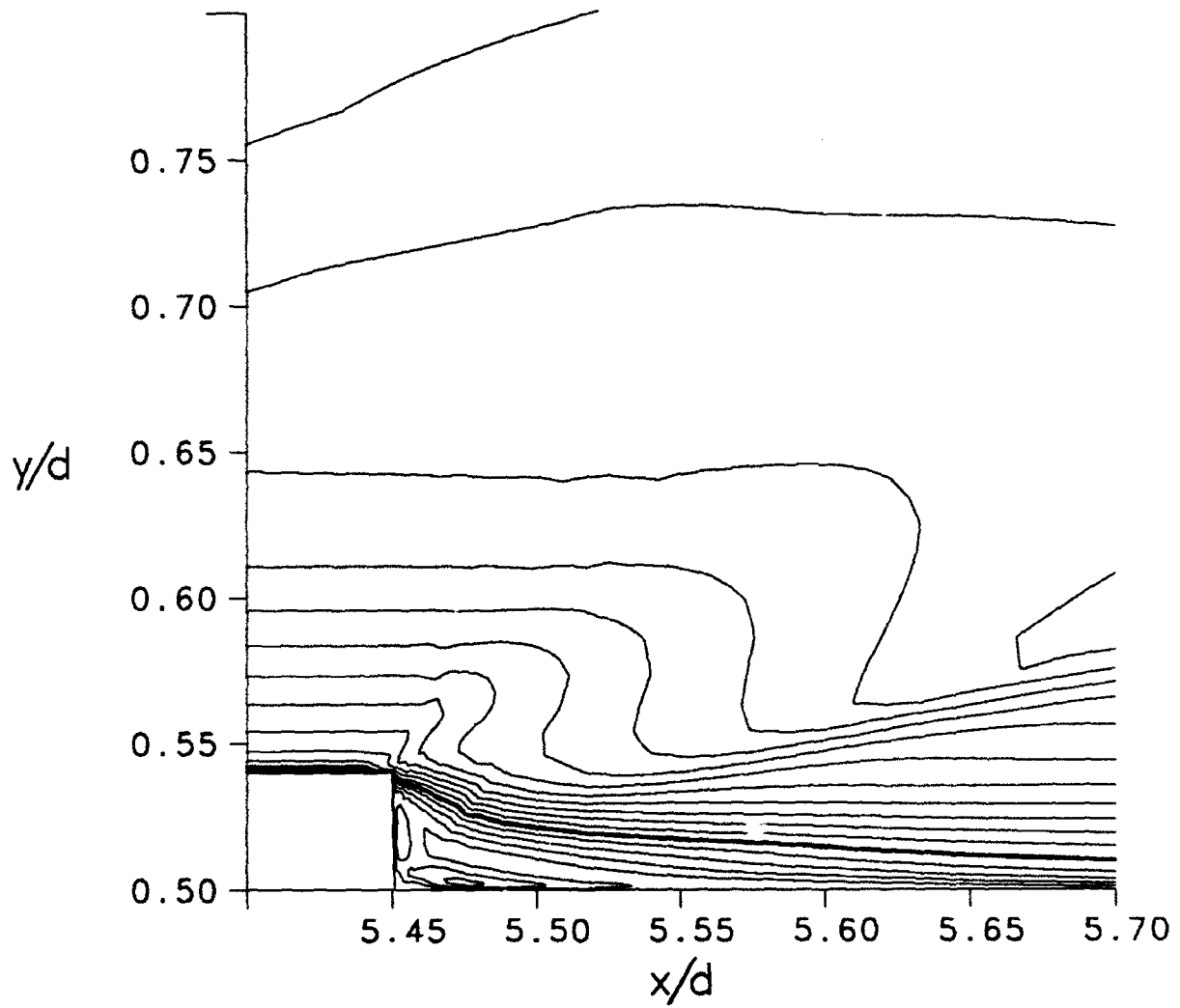


Figure 9. Computed Mach Contours near Rearward Face, $M=3.0$ (0.1 to 3.0 in increments of 0.1)

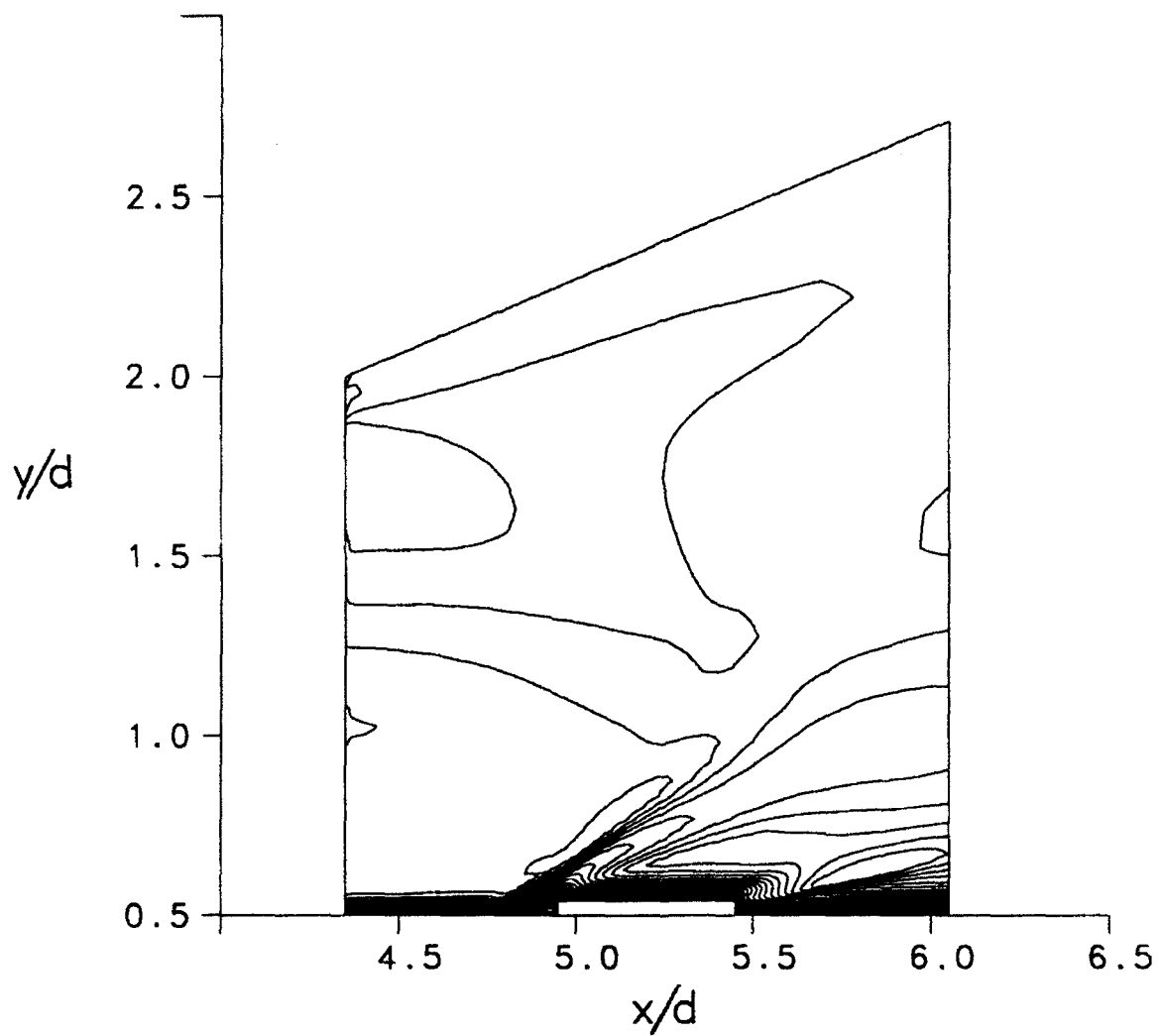


Figure 10. Computed Mach Contours, $M=3.0$ (0.1 to 3.2 in increments of 0.1)

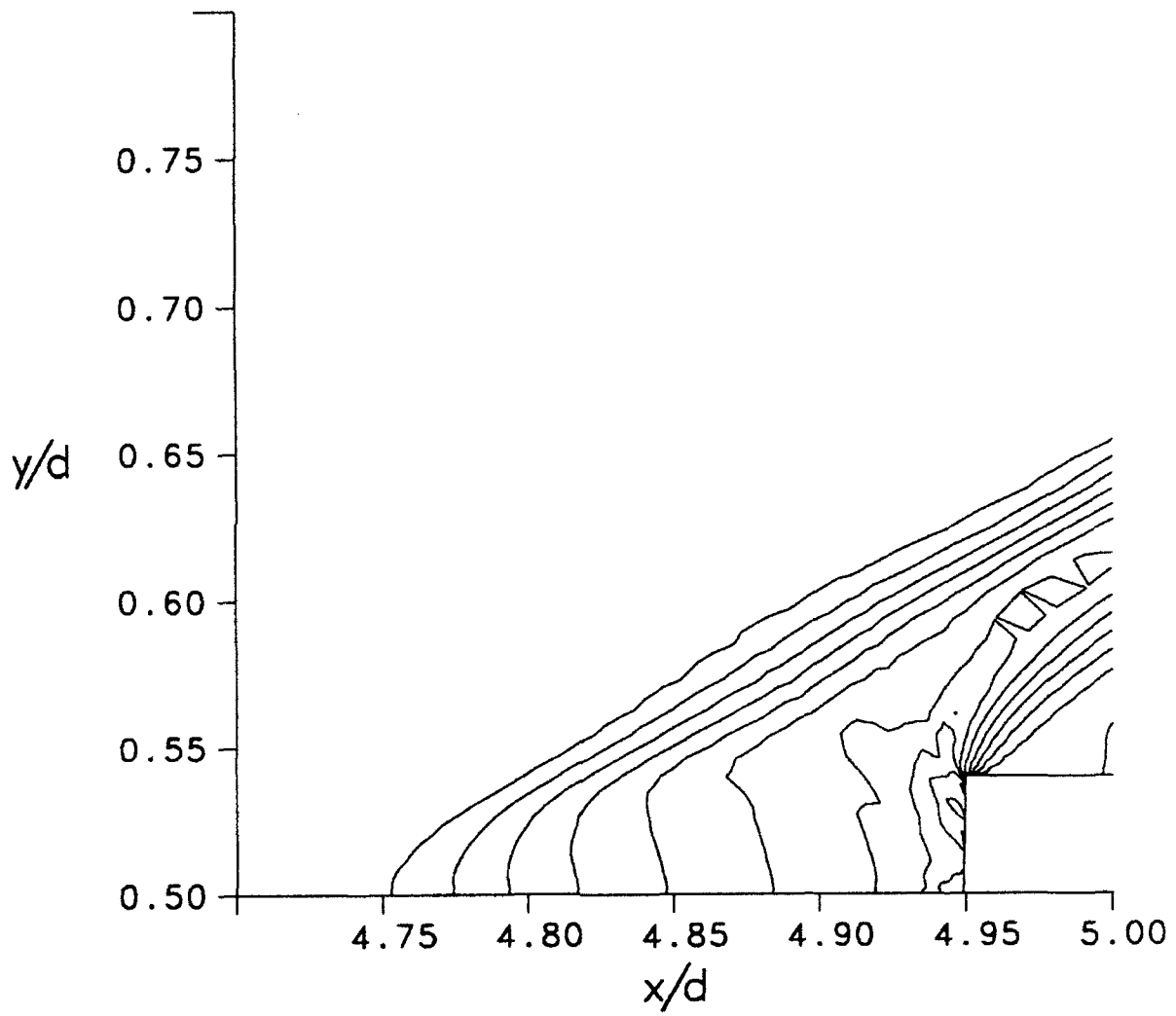


Figure 11. Computed Pressure Contours near Forward Face, $M=3.0$ (1.1 to 2.9 in increments of 0.2)

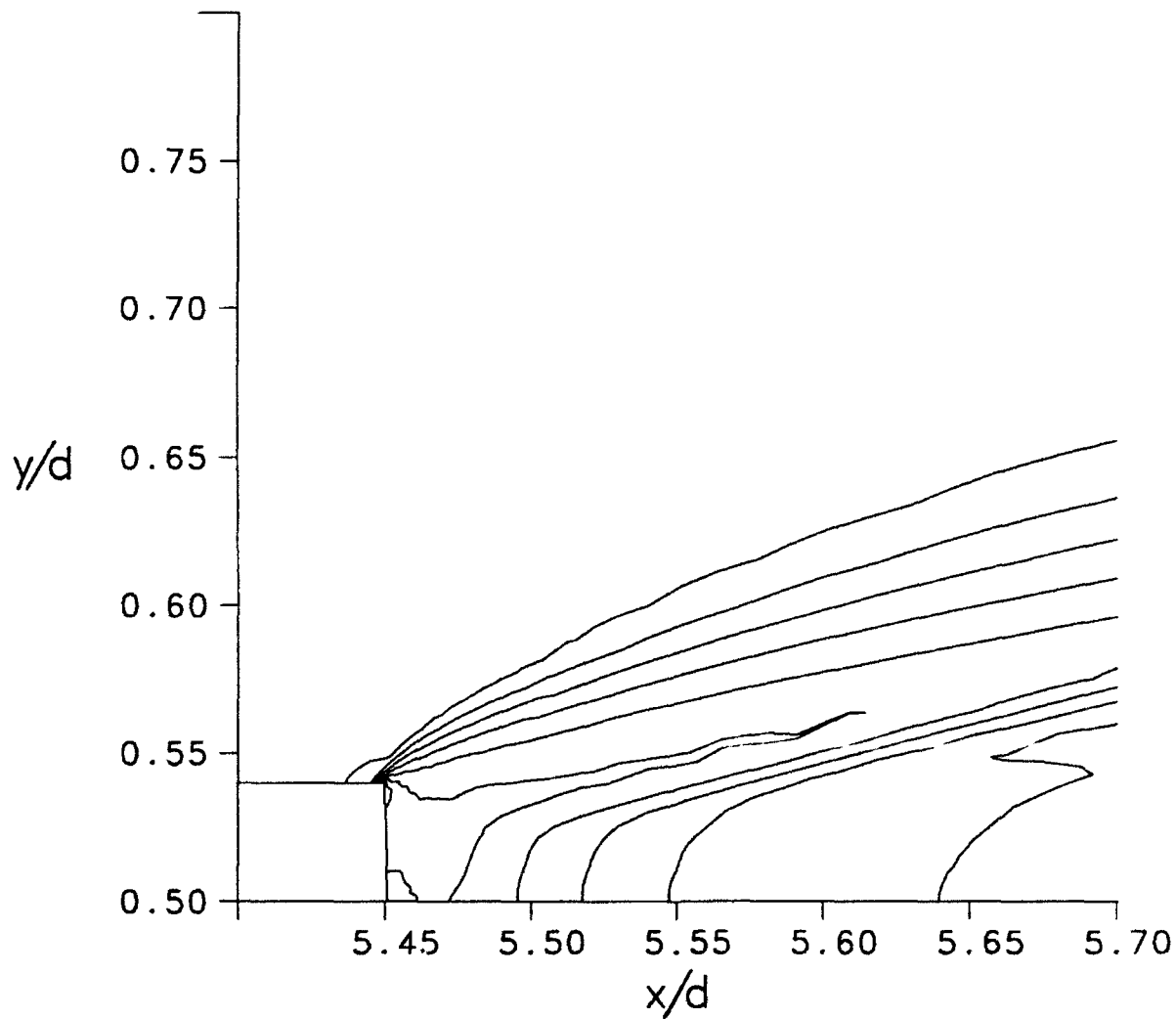


Figure 12. Computed Pressure Contours near Rearward Face, $M=3.0$ (0.2 to 0.8 in increments of 0.1)

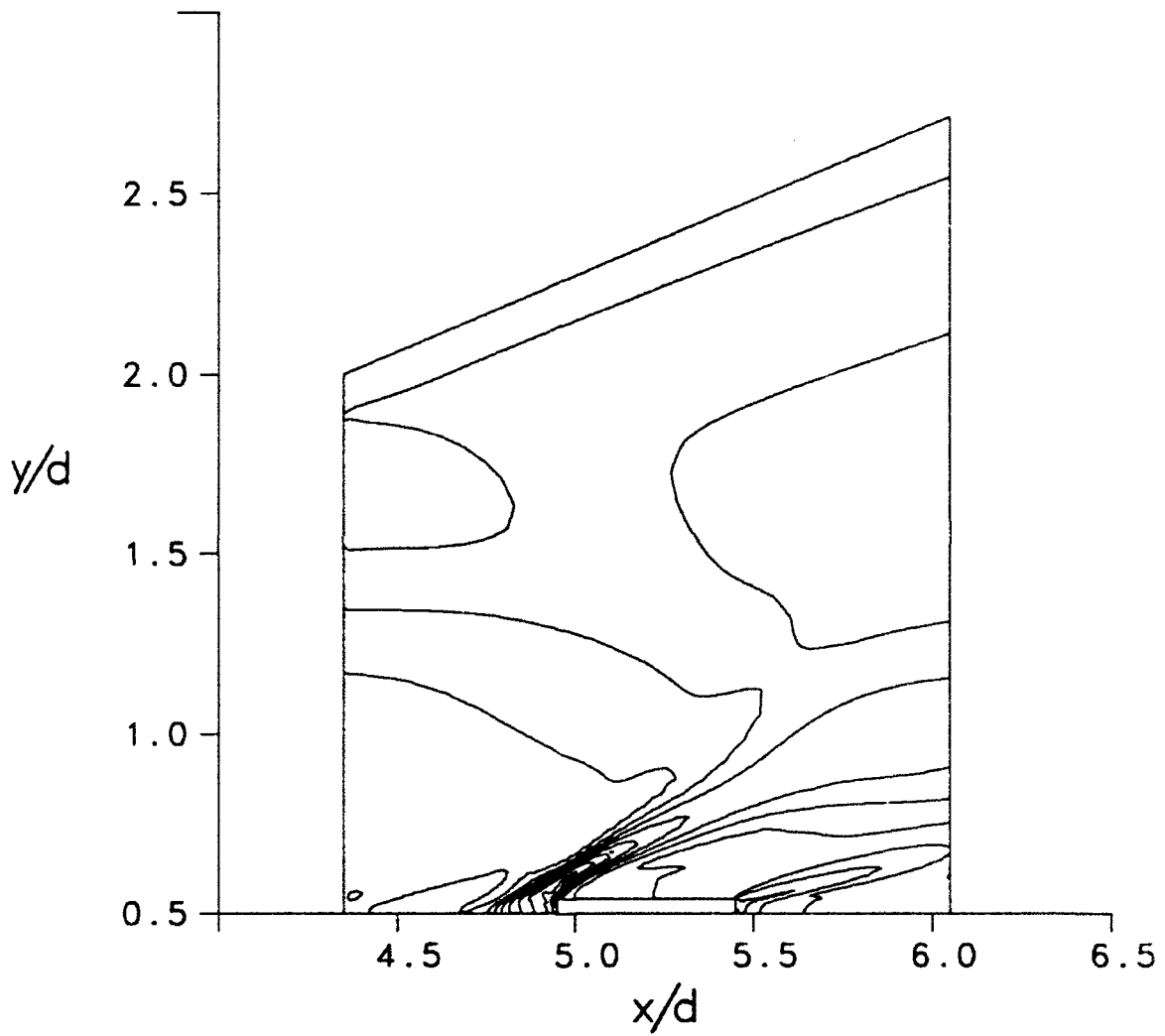


Figure 13. Computed Pressure Contours, $M=3.0$ (0.1 to 3.0 in increments of 0.1)

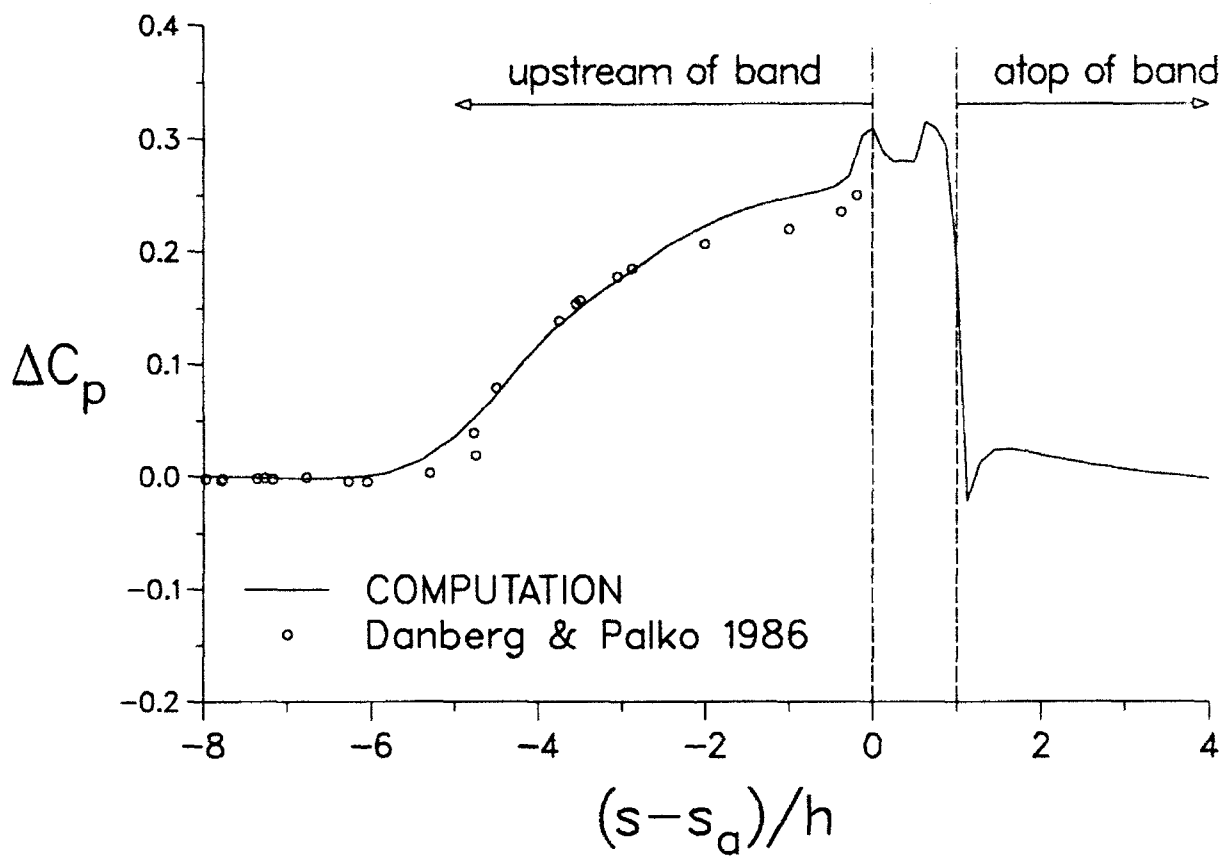


Figure 14. Surface Pressure Comparison near Forward Face, $M=2.5$

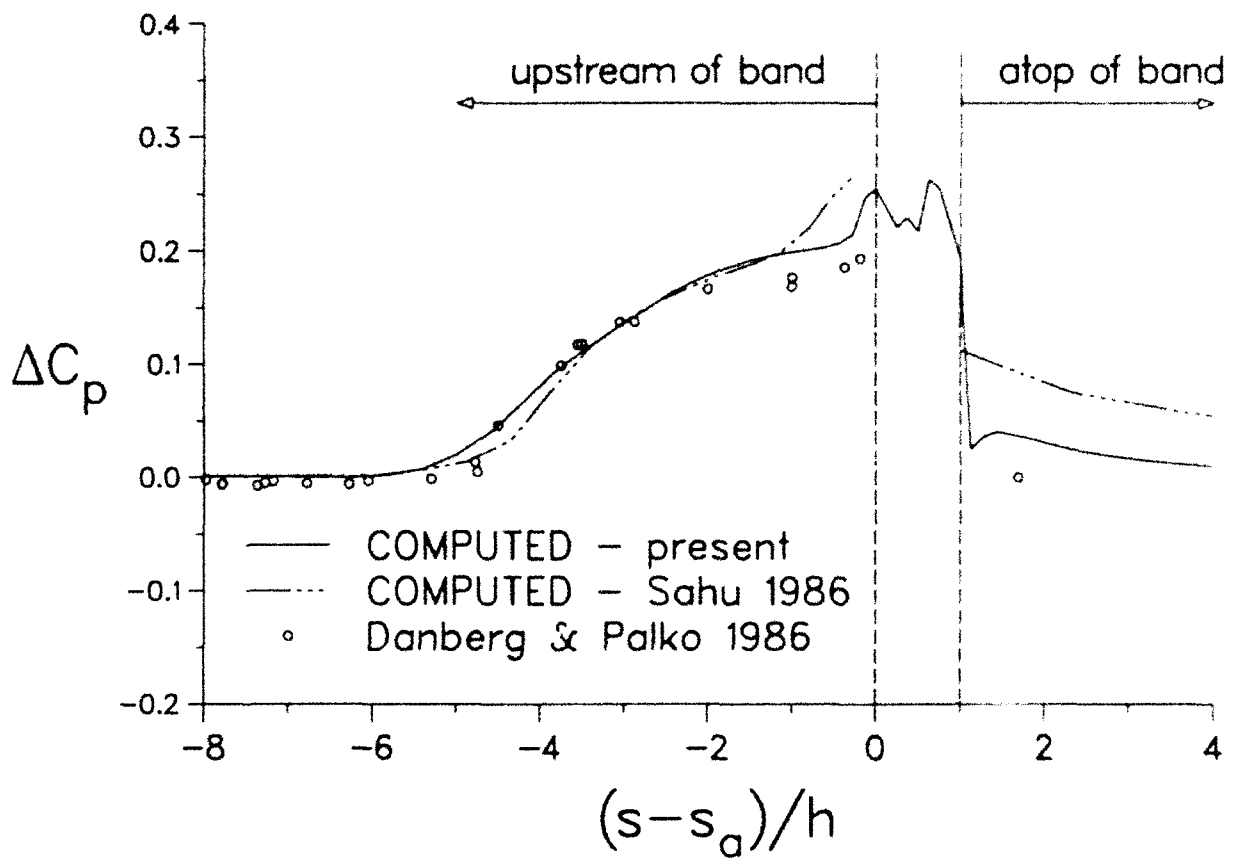


Figure 15. Surface Pressure Comparison near Forward Face, $M=3.0$

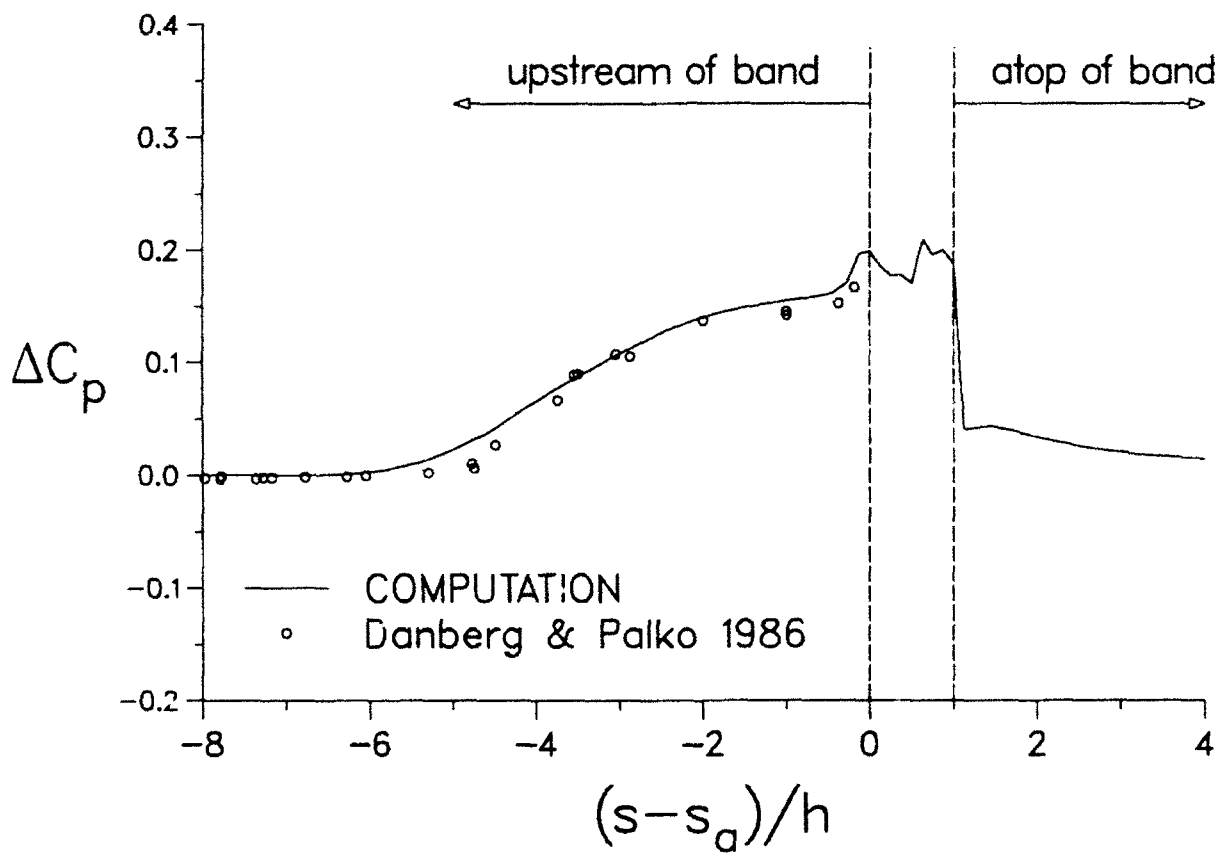


Figure 16. Surface Pressure Comparison near Forward Face, $M=3.5$

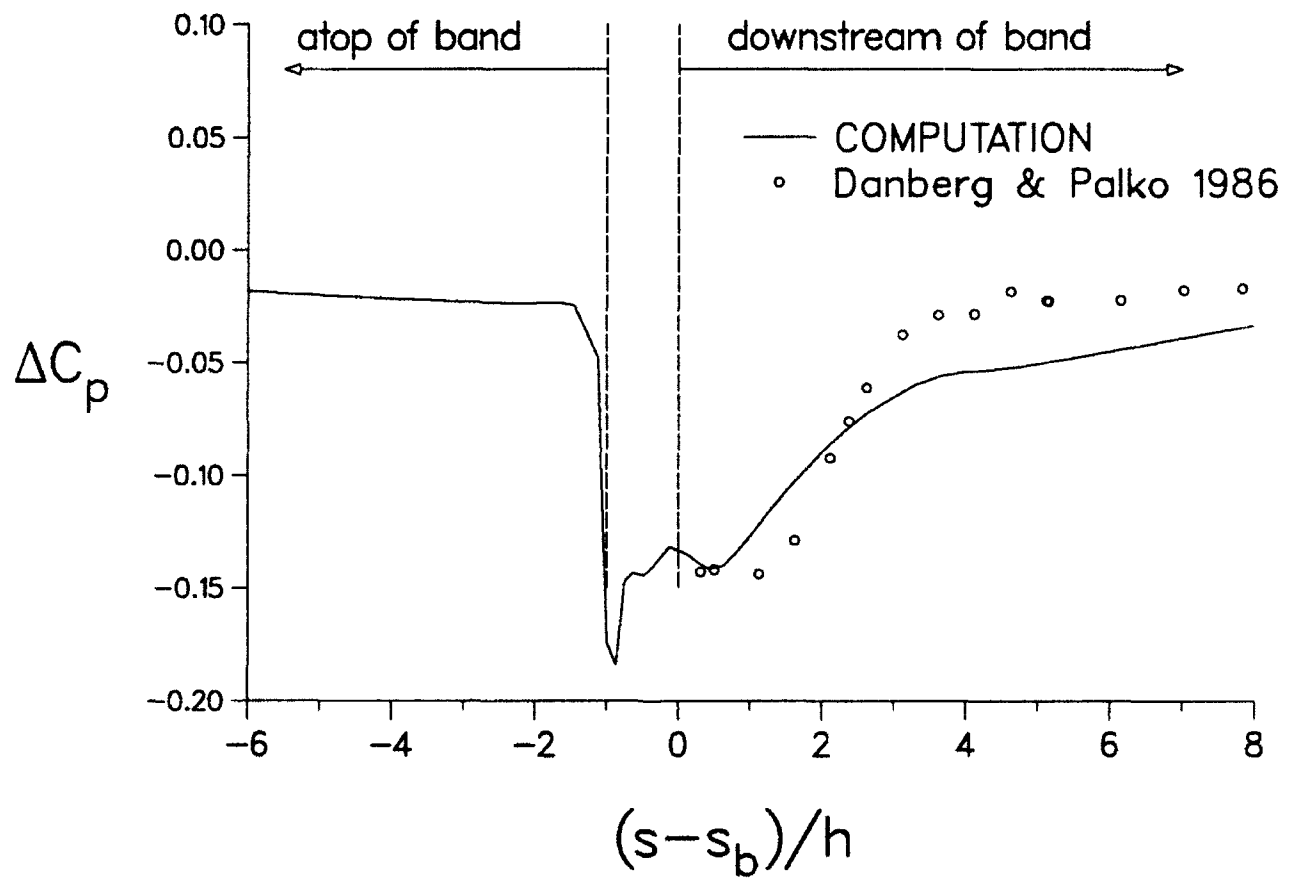


Figure 17. Surface Pressure Comparison near Rearward Face, $M=2.5$

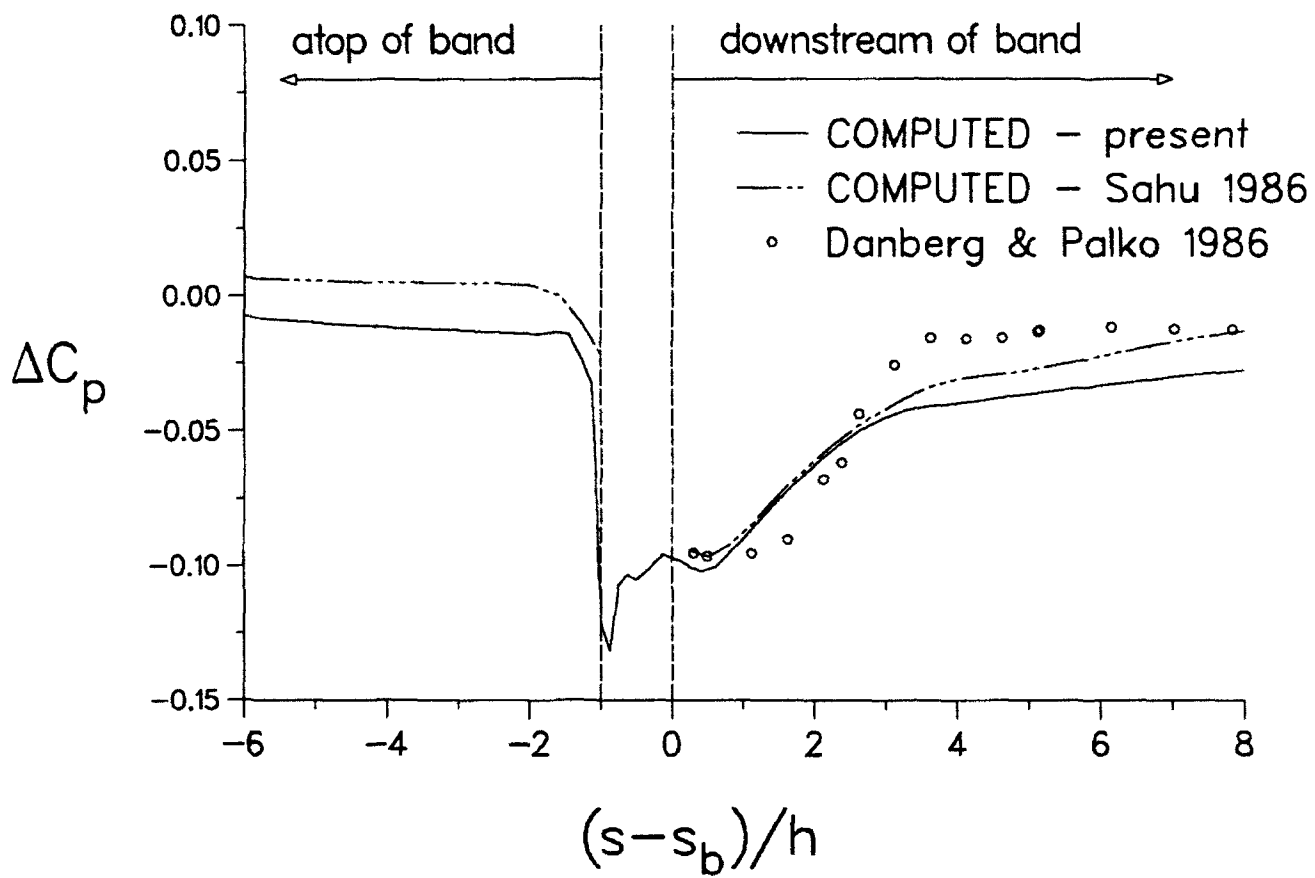


Figure 18. Surface Pressure Comparison near Rearward Face, $M=3.0$

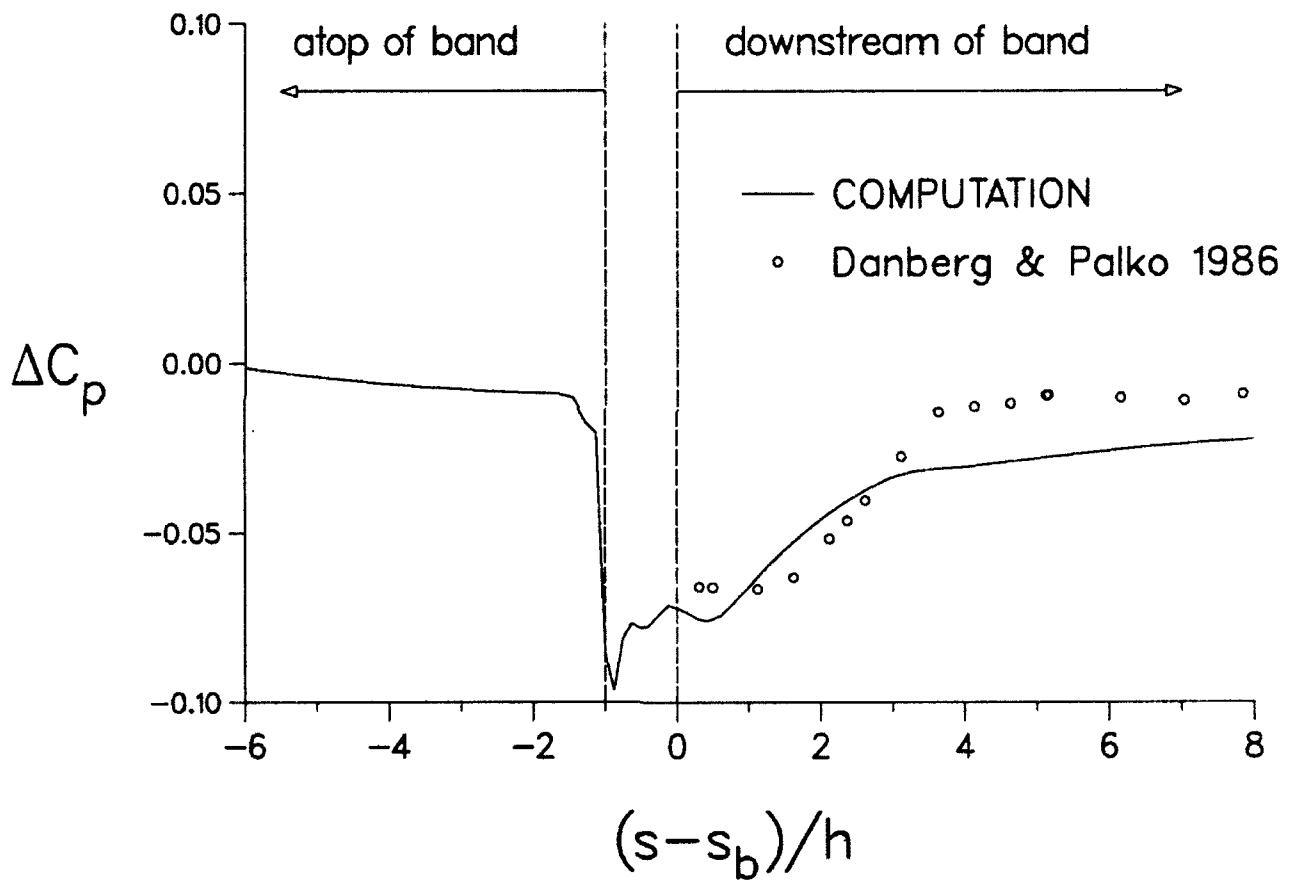


Figure 19. Surface Pressure Comparison near Rearward Face, $M=3.5$

INTENTIONALLY LEFT BLANK.

7. REFERENCES

- Baldwin, B.S., and H. Lomax. "Thin-Layer Approximation and Algebraic Model for Separated Turbulent Flows." AIAA Paper No. 78-0257, January 1978.
- Beam, R. and R.F. Warming. "An Implicit Factored Scheme for the Compressible Navier-Stokes Equations." AIAA Journal, Vol. 16, No. 4, pp 85-129, 1978.
- Danberg, J.E. "Numerical Modeling of Rotating Band Flow Field and Comparison with Experiment." U.S. Army Ballistic Research Laboratory, Aberdeen Proving Ground, Maryland, ARBRL-TR-02505, July 1983. (AD 131260)
- Danberg, J.E., and K.L. Palko. "Measurement of Surface Pressures Caused by a Projectile Rotating Band at Supersonic Speeds." U.S. Army Ballistic Research Laboratory, Aberdeen Proving Ground, Maryland, BRL-MR-3532, July 1986. (AD A171082)
- Danberg, J.E., and N.R. Patel. "An Algebraic Turbulence Model For Flow Separation Caused by Forward and Backward Facing Steps." U.S. Army Ballistic Research Laboratory, Aberdeen Proving Ground, Maryland, BRL-MR-3791, December 1989. (AD 213800)
- Gorney, J.L., W.J. Yanta, and D.W. Ausherman. "Laser Doppler Velocimeter Measurements of the Two-Dimensional Boundary Layers on a Projectile Shape at Mach 3." NSWC MP 82-430, Naval Surface Weapons Center, Silver Spring, Maryland, September 1982.
- Kutler, P., S. Chakravarthy, and C.K. Lombard. "Supersonic Flow over Ablated Nostetips using an Unsteady, Implicit, Numerical Procedure." AIAA Paper 78-213, January 1978.
- McCoy, R.L. " 'McDrag'- A Computer Program for Estimating the Drag Coefficients of Projectiles." U.S. Army Ballistic Research Laboratory / ARRADCOM, Aberdeen Proving Ground, Maryland, ARBRL-TR-02293, February 1981. (AD A09810)
- Pulliam, T.H., and J.L. Steger. "On Implicit Finite-Difference Simulations of Three Dimensional Flow." AIAA Paper No. 78-0010, January 1978.
- Rai, M.M., and D.S. Chaussee. "New Implicit Boundary Procedures: Theory and Applications." AIAA Paper No. 83-0123, January 1983.
- Rizk, Y.M., D.S. Chaussee, and D.S. McRae. "Numerical Simulation of Viscous-Inviscid Interactions on Indented Nostetips." AIAA Paper No. 82-0290, January 1982.
- Sahu, J. "Numerical Simulation of Supersonic Flow over a Rotating Band using Flowfield Blanking." U.S. Army Ballistic Research Laboratory, Aberdeen Proving Ground, Maryland, BRL-MR-3561, December 1986. (AD 178492)
- Schiff, L.B., and J.L. Steger. "Numerical Simulation of Steady Supersonic Flow." AIAA Paper No. 79-0130, January 1979.
- Schiff, L.B., and W.B. Sturek. "Numerical Simulation of Steady Supersonic Flow over an Ogive Cylinder Boattail Body." U.S. Army Ballistic Research Laboratory, Aberdeen Proving Ground, Maryland, ARBRL-TR-02363, September 1981. (AD 106060)
- Sedney, R. "A Survey of the Effects of Small Protuberances on Boundary-Layer Flows." AIAA Journal, Vol. 11, No. 6, pp 728-792, June 1973.

- Steger, J.L., and R.L. Sorenson. "Automatic Mesh-Point Clustering Near a Boundary in Grid Generation with Elliptic Partial Differential Equations." Journal of Computational Physics, Vol. 33, pp 405-410, 1979.
- Sturek, W.B., and L.B. Schiff. "Computations of Magnus Effect for Slender Bodies in Supersonic Flow." U.S. Army Ballistic Research Laboratory, Aberdeen Proving Ground, Maryland, ARBRL-TR-02384, December 1981. (AD A110016)
- Thompson, J.F., F.C. Thames, and C.W. Mastin. "Automatic Numerical Generation of Body-Fitted Curvilinear Coordinate System for Field Containing any Number of Arbitrary Geometries." Journal of Computational Physics, Vol. 15, pp 299-319, 1974.
- Weinacht, P., B.J. Guidos, and L.D. Kayser. Sturek, W.B., "PNS Computations for Spinning and Fin-Stabilized Projectiles at Supersonic Speeds." U.S. Army Ballistic Research Laboratory, Aberdeen Proving Ground, Maryland, ARBRL-MR-3464, September 1985. (AD A160393)
- Young, A.D., and J.H. Paterson. "Aircraft Excrescence Drag." AGARD-AG-264, 1981.

**APPENDIX:
TABULATED SURFACE PRESSURE DATA**

$M=2.5$			
upstream of band		downstream of band	
$(s - s_a)/h$	$\Delta C_p \times 10^2$	$(s - s_b)/h$	$\Delta C_p \times 10^2$
-14.9	-0.001	0.312	-0.142
-15.6	-0.001	0.500	-0.142
-14.4	-0.001	1.125	-0.144
-13.9	-0.004	1.625	-0.129
-12.9	-0.005	2.125	-0.092
-12.8	-0.003	2.375	-0.075
-12.4	-0.009	2.625	-0.061
-12.4	-0.005	3.125	-0.037
-11.4	-0.003	3.625	-0.029
-10.5	-0.002	4.125	-0.028
-9.59	-0.004	4.625	-0.018
-9.40	-0.002	5.125	-0.023
-8.77	-0.002	5.150	-0.023
-8.60	-0.002	6.150	-0.022
-8.28	-0.003	7.025	-0.018
-7.97	-0.002	7.837	-0.017
-7.79	-0.004	8.025	-0.014
-7.78	-0.002	8.650	-0.014
-7.36	-0.002	8.900	-0.010
-7.26	-0.001	9.150	-0.012
-7.17	-0.002	9.525	-0.011
-6.78	-0.006	9.650	-0.009
-6.26	-0.005	9.713	-0.010
-6.04	-0.005	10.15	-0.007
-5.30	0.003	10.65	-0.006
-4.78	0.039	11.15	-0.007
-4.75	0.019	12.65	-0.006
-4.50	0.079	12.67	-0.002
-3.75	0.138	13.00	-0.004
-3.55	0.153	13.67	-0.001
-3.50	0.156	14.00	-0.004
-3.05	0.177	14.55	0.0003
-2.86	0.184	15.50	-0.004
-2.00	0.206	16.42	0.0002
-1.00	0.219	17.05	0.0009
-0.38	0.235	17.12	-0.006
-0.19	0.249	17.24	-0.00003

$M=3.0$			
upstream of band		downstream of band	
$(s - s_a)/h$	$\Delta C_p \times 10^2$	$(s - s_b)/h$	$\Delta C_p \times 10^2$
-14.9	-0.002	0.313	-0.095
-14.6	-0.004	0.500	-0.097
-14.4	-0.001	1.125	-0.095
-13.9	-0.003	1.625	-0.090
-13.0	-0.003	2.125	-0.067
-12.8	-0.003	2.375	-0.062
-12.4	-0.004	2.625	-0.044
-12.4	-0.002	3.125	-0.026
-11.4	-0.002	3.625	-0.016
-10.5	-0.002	4.125	-0.016
-9.59	-0.006	4.625	-0.015
-9.40	-0.007	5.125	-0.013
-8.78	-0.005	5.150	-0.013
-8.60	-0.003	6.150	-0.012
-8.59	-0.002	7.025	-0.012
-8.28	-0.006	7.837	-0.013
-7.97	-0.002	8.025	-0.012
-7.79	-0.006	8.650	-0.011
-7.78	-0.006	8.898	-0.013
-7.36	-0.007	8.900	-0.011
-7.28	-0.005	9.150	-0.011
-7.17	-0.003	9.525	-0.010
-6.78	-0.005	9.650	-0.010
-6.28	-0.006	9.713	-0.014
-6.05	-0.003	10.15	-0.007
-5.30	0.001	10.65	-0.008
-4.78	0.005	11.15	-0.009
-4.75	0.046	12.65	-0.005
-4.50	0.099	12.67	-0.004
-3.75	0.118	13.00	-0.004
-3.55	0.118	13.67	-0.0001
-3.50	0.138	14.00	-0.001
-3.05	0.138	14.55	-0.0004
-2.88	0.167	15.50	-0.002
-2.00	0.169	16.42	-0.001
-1.00	0.177	16.42	0.002
-0.38	0.186	17.05	0.002
-0.19	0.194	17.13	-0.001

$M=3.5$			
upstream of band		downstream of band	
$(s - s_a)/h$	$\Delta C_p \times 10^2$	$(s - s_b)/h$	$\Delta C_p \times 10^2$
-14.9	-0.002	0.312	-0.065
-14.6	-0.002	0.500	-0.066
-14.4	-0.002	1.125	-0.067
-13.9	-0.002	1.625	-0.063
-12.9	-0.002	2.125	-0.052
-12.8	-0.009	2.375	-0.046
-12.4	-0.003	2.625	-0.040
-12.4	-0.003	3.125	-0.027
-11.4	-0.002	3.625	-0.014
-10.5	-0.001	4.125	-0.013
-9.59	-0.003	4.625	-0.012
-9.40	-0.003	5.125	-0.009
-8.78	-0.002	5.150	-0.009
-8.60	-0.002	6.150	-0.010
-8.59	-0.002	7.025	-0.011
-8.28	-0.002	7.837	-0.009
-7.97	-0.004	8.025	-0.009
-7.79	-0.002	8.650	-0.009
-7.78	-0.001	8.898	-0.011
-7.36	-0.003	8.900	-0.011
-7.26	-0.003	9.150	-0.008
-7.17	-0.002	9.525	-0.011
-6.78	-0.002	9.650	-0.009
-6.28	-0.002	9.713	-0.010
-6.05	-0.001	10.15	-0.009
-5.30	-0.0007	10.65	-0.009
-4.78	0.003	11.14	-0.009
-4.75	0.010	12.65	-0.009
-4.50	0.006	12.67	-0.007
-3.75	0.027	13.00	-0.008
-3.55	0.066	13.67	-0.005
-3.50	0.089	14.00	-0.006
-3.05	0.107	14.55	-0.007
-2.88	0.106	15.50	-0.004
-2.00	0.137	16.42	-0.003
-1.01	0.146	16.42	-0.003
-1.00	0.142	17.05	-0.003
-0.38	0.153	17.13	-0.003
-0.18	0.167	17.24	-0.002

INTENTIONALLY LEFT BLANK.

LIST OF SYMBOLS

a	speed of sound
C_p	surface pressure coefficient
C_t	Courant number
c_p	constant pressure specific heat
d	reference diameter of body of revolution (equal to 1 caliber)
$\hat{E}_s, \hat{E}, \hat{F}, \hat{G}$	inviscid flux vectors of transformed gas dynamic equations
h	rotating band thickness (protuberance or step height)
i, j, k	grid point indices associated with ξ, η, ζ , respectively
J	Jacobian of coordinate transformation
L	reference length (equal to 1 caliber)
M	free-stream Mach number
p	pressure
\bar{Q}	vector of dependent variables of gas dynamic equations
\hat{Q}	vector of dependent variables of transformed gas dynamic equations
Re	Reynolds number, $\rho_\infty u_\infty L / \mu_\infty$
\hat{Re}	sonic Reynolds number, $\rho_\infty a_\infty L / \mu_\infty$
r	radial coordinate
\hat{S}	viscosity vector of transformed gas dynamic equations
s	arc length in ξ direction
t	time
u, v, w	velocity components in x, y, z directions
\tilde{u}	velocity component close to and parallel to wall
x, y, z	physical Cartesian coordinates
\tilde{y}	normal distance from wall

Greek Symbols

γ	ratio of specific heats
δ^*	boundary layer displacement thickness
ϵ_i, ϵ_e	implicit and explicit numerical damping parameters
ϵ	total energy per unit volume of fluid
μ	coefficient of molecular viscosity
ρ	density
τ	transformed coordinate of time
θ	angle of grid orthogonality
ξ, η, ζ	transformed coordinates

Subscripts

a	evaluated at bottom corner of forward facing step
b	evaluated at bottom corner of rearward facing step
e	boundary layer edge condition
$reat$	evaluated at flow reattachment location

sep evaluated at flow separation location
w wall condition
 ∞ free-stream condition
 $|_f$ evaluated at *f*

<u>No. of</u> <u>Copies</u>	<u>Organization</u>	<u>No. of</u> <u>Copies</u>	<u>Organization</u>
2	Administrator Defense Technical Info Center ATTN: DTIC-DDA Cameron Station Alexandria, VA 22304-6145	1	Commander U.S. Army Missile Command ATTN: AMSMI-RD-CS-R (DOC) Redstone Arsenal, AL 35898-5010
1	Commander U.S. Army Materiel Command ATTN: AMCAM 5001 Eisenhower Ave. Alexandria, VA 22333-0001	1	Commander U.S. Army Tank-Automotive Command ATTN: ASQNC-TAC-DIT (Technical Information Center) Warren, MI 48397-5000
1	Director U.S. Army Research Laboratory ATTN: AMSRL-D 2800 Powder Mill Rd. Adelphi, MD 20783-1145	1	Director U.S. Army TRADOC Analysis Command ATTN: ATRC-WSR White Sands Missile Range, NM 88002-5502
1	Director U.S. Army Research Laboratory ATTN: AMSRL-OP-CI-AD, Tech Publishing 2800 Powder Mill Rd. Adelphi, MD 20783-1145	1	Commandant U.S. Army Field Artillery School ATTN: ATSF-CSI Fl. Sill, OK 73503-5000
2	Commander U.S. Army Armament Research, Development, and Engineering Center ATTN: SMCAR-IMI-I Picatinny Arsenal, NJ 07806-5000	(Class. only) 1	Commandant U.S. Army Infantry School ATTN: ATSH-CD (Security Mgr.) Fort Benning, GA 31905-5660
2	Commander U.S. Army Armament Research, Development, and Engineering Center ATTN: SMCAR-TDC Picatinny Arsenal, NJ 07806-5000	(Unclass. only) 1	Commandant U.S. Army Infantry School ATTN: ATSH-CD-CSO-OR Fort Benning, GA 31905-5660
1	Director Benet Weapons Laboratory U.S. Army Armament Research, Development, and Engineering Center ATTN: SMCAR-CCB-TL Watervliet, NY 12189-4050	1	WL/MNOI Eglin AFB, FL 32542-5000 <u>Aberdeen Proving Ground</u>
(Unclass. only) 1	Commander U.S. Army Rock Island Arsenal ATTN: SMCRI-IMC-RT/Technical Library Rock Island, IL 61299-5000	2	Dir, USAMSAA ATTN: AMXSU-D AMXSU-MP, H. Cohen
1	Director U.S. Army Aviation Research and Technology Activity ATTN: SAVRT-R (Library) M/S 219-3 Ames Research Center Moffett Field, CA 94035-1000	1	Cdr, USATECOM ATTN: AMSTE-TC
		1	Dir, ERDEC ATTN: SCBRD-RT
		1	Cdr, CBDA ATTN: AMSCB-CI
		1	Dir, USARL ATTN: AMSRL-SL-I
		10	Dir, USARL ATTN: AMSRL-OP-CI-B (Tech Lib)

<u>No.</u> <u>Copies</u>	<u>Organization</u>	<u>No.</u> <u>Copies</u>	<u>Organization</u>
10	Commander US Army Armament R,D&E Center ATTN: SMCAR-AET-A R. Kline S. Kahn C. Ng M. Amoruso H. Hudgins J. Grau F. Brown B. Wong W. Toledo S. Chung Picatinny Arsenal, NJ 07806-5000	1	United States Military Academy Department of Mechanics ATTN: LTC Andrew L. Lull West Point, NY 10996
		3	Air Force Armament Laboratory ATTN: AFATL/FXA B. Simpson G. Abate R. Adelgren Eglin AFB, FL 32542-5434
		2	Institute for Advanced Technology University of Texas at Austin ATTN: W. Reinecke T. Kiehne 4030-2 W. Braker Lane Austin, TX 78759-5329
2	Commander Naval Surface Warfare Center Applied Mathematics Branch ATTN: Code R44 (F. Priolo) Code R44 (A. Wardlaw) White Oak Laboratory Silver Spring, MD 20903-5000	6	Director National Aeronautics and Space Administration Ames Research Center ATTN: MS-258-1, L. Schiff MS-258-1, T. Holst MS-258-1, D. Chaussee MS-258-1, T. Edwards MS-258-1, G. Molvik MS-258-1, S. Lawrence Moffett Field, CA 94035
1	Commander US Army Missile Command ATTN: AMSMI-RD-SS-AT B. Walker Redstone Arsenal, AL 35898-5010		
3	Director National Aeronautics and Space Administration Langley Research Center ATTN: Tech Library J. South M.M. Rai Langley Station Hampton, VA 23665	1	Commander US Naval Surface Weapons Center ATTN: F. Moore Dahlgren, VA 22448
		2	USAF Wright Aeronautical Laboratories ATTN: AFWAL/FIMG J. Shang WPAFB, OH 45433-6553

<u>No.</u>	<u>Organization</u>
1	AEDC Calspan Field Service ATTN: MS 600 (J. Benek) AAFS, TN 37389
2	Director Sandia National Laboratories ATTN: W.L. Oberkampf W. Wolfe Division 1636 Albuquerque, NM 87185
1	MDA Engineering, Inc. ATTN: J. P. Steinbrenner 500 E. Border St. Suit 401 Arlington, TX 76010
1	Los Alamos National Laboratory ATTN: Bill Hogan MS G770 Los Alamos, NM 87545
1	Southwest Research Institute ATTN: David L. Littlefield San Antonio, TX 78228-0510
2	University of California, Davis Department of Mechanical Engineering ATTN: H.A. Dwyer B. Meakin Davis, CA 95616
1	University of Maryland Department of Aerospace Engr. ATTN: J. D. Anderson, Jr. College Park, MD 20742

<u>No.</u>	<u>Organization</u>
1	University of Texas Department of Aerospace Engineering and Engineering Mechanics ATTN: D. S. Dolling Austin, Texas 78712-1055
1	University of Delaware Department of Mechanical Engineering ATTN: L. Schwartz Newark, DE 19716
1	University of Cincinnati Department of Aerospace Engineering ATTN: S. Rubin Mail Location 70 Cincinnati, OH 45221
1	University of Florida Department of Engineering Sciences College of Engineering ATTN: C. C. Hsu Gainesville, FL 32611
2	Alliant Techsystems, Inc. ATTN: M. Swenson R. Burretta Mail Station MN48-3700 7225 Northland Dr. Brooklyn Park, MN 55428
2	Director US Army ERDEC ATTN: SCBRD-RTB D. Weber F. Wrede Aberdeen Proving Ground, MD 21010-5423

INTENTIONALLY LEFT BLANK.

USER EVALUATION SHEET/CHANGE OF ADDRESS

This Laboratory undertakes a continuing effort to improve the quality of the reports it publishes Your comments/answers to the items/questions below will aid us in our efforts.

1. ARL Report Number ARL-TR-102 Date of Report March 1993

2. Date Report Received _____

3. Does this report satisfy a need? (Comment on purpose, related project, or other area of interest for which the report will be used.) _____

4. Specifically, how is the report being used? (Information source, design data, procedure, source of ideas, etc.) _____

5. Has the information in this report led to any quantitative savings as far as man-hours or dollars saved, operating costs avoided, or efficiencies achieved, etc? If so, please elaborate. _____

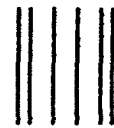
6. General Comments. What do you think should be changed to improve future reports? (Indicate changes to organization, technical content, format, etc.) _____

CURRENT ADDRESS Organization _____ Name _____ Street or P.O. Box No. _____ City, State, Zip Code _____

7. If indicating a Change of Address or Address Correction, please provide the Current or Correct address above and the Old or Incorrect address below.

OLD ADDRESS Organization _____ Name _____ Street or P.O. Box No. _____ City, State, Zip Code _____

DEPARTMENT OF THE ARMY



OFFICIAL BUSINESS

BUSINESS REPLY MAIL
FIRST CLASS PERMIT No 0001, APG, MD

Postage will be paid by addressee

NO POSTAGE
NECESSARY
IF MAILED
IN THE
UNITED STATES



Director
U.S. Army Research Laboratory
ATTN: AMSRL-OP-CI-B (Tech Lib)
Aberdeen Proving Ground, MD 21005-5066